

Normal modes of cold confined one-component plasmas

Daniel H. E. Dubin

Department of Physics, University of California at San Diego, La Jolla, California 92093-0319

J. P. Schiffer

Argonne National Laboratory, Argonne, Illinois 60439

and University of Chicago, Chicago, Illinois 60637

(Received 10 May 1995)

It is possible to trap a collection of ions and cool them to cryogenic temperatures where strong correlation effects, such as transitions to liquid and crystalline states, are observed. This paper examines the effect of correlations on the linear normal modes of oscillation in these strongly coupled plasmas. Recently a theory has been developed to treat such modes in the cold-fluid limit, where correlations are neglected. Here the fluid theory is compared to molecular-dynamics simulations of the modes. Simulated mode frequencies are observed to shift slightly compared to the cold-fluid predictions, and the modes are also observed to damp in time. Unmagnetized simulations also reveal a set of torsional oscillations which have no counterpart in the fluid theory. These correlation effects are also compared to a recently developed model that treats the trapped plasma as a viscoelastic spheroid. The model allows us to extract from the simulations the values of high-frequency bulk and shear moduli of a strongly correlated plasma. [S1063-651X(96)03805-6]

PACS number(s): 52.25.Wz, 32.80.Pj, 52.35.Fp, 62.20.Dc

I. INTRODUCTION

It has recently been demonstrated that electromagnetic fields can be employed to trap a collection of charges of a single species for long periods of time. Using the technique of laser cooling, the charges can be cooled to extremely low temperatures on the order of a few mK. Although the mean distance between charges is large (on the order of microns) the temperature is sufficiently small so that the ratio of average interaction energy to kinetic energy per charge, $\Gamma \equiv q^2/(a_{\text{WS}}kT)$, is larger than unity. [Here T is the temperature, k is Boltzmann's constant, q is the charge, and a_{WS} is the average interparticle spacing (the Wigner-Seitz radius) defined in terms of the mean density n_0 by $4\pi n_0 a_{\text{WS}}^3/3 = 1$.] The parameter Γ is referred to as the correlation parameter. In the regime $\Gamma > 1$, the system exhibits phenomena associated with the physics of strong correlation, such as transitions to liquid or even solid phases. These correlation phenomena have been extensively studied in a series of computer simulations relevant to different trap configurations [1–3], and were later observed in actual experiments in (magnetic) Penning traps [4] and in (radio-frequency) Paul traps [5].

At the cryogenic temperatures of the experiments the Debye length $\lambda_D \equiv \sqrt{kT/(4\pi q^2 n_0)}$ is usually small compared to the size of the charge cloud, so the cloud can exhibit collective oscillations associated with non-neutral plasmas, even though the number of trapped particles is often quite small, $N \lesssim 10^4$. While the collective modes of non-neutral plasmas have been studied for decades [6], certain aspects have only recently been investigated. For example, when the plasma cloud is small the low-order modes are the most easily excited, but the frequency of these modes depends on the plasma shape. Furthermore, an accurate description of the shape dependence is desirable since measurement of the modes then provides a nondestructive diagnostic of the shape

as well as other properties of the plasma. Recently, a theory [7] for the collective modes of a small spheroidal plasma has been developed which agrees well with experimental measurements [8,9] of some of the normal mode frequencies of trapped charge clouds. However, the theory treats the cloud as a charged cold fluid, neglecting the granularity associated with interparticle correlations.

In this paper we consider the effect of the interparticle correlations on low-order normal modes of the trapped charge cloud. Using molecular-dynamics (MD) simulations, we find that low-order mode frequencies are described well by the aforementioned cold-fluid theory for clouds as small as 100 charges, even when the cloud has crystallized. We also find that slight frequency differences between the simulated modes and the fluid theory are systematic, and can be explained by physical effects associated with strong correlation. In addition to the slight frequency shifts observed in the simulated normal modes, we also observe mode damping which is consistent with viscous effects due to collisions in the strongly correlated plasmas.

The frequency shifts and damping of the low-order modes can be explained in detail using a viscoelastic model [10] of the cloud based on the bulk dynamical properties of a homogeneous one-component plasma (OCP). The OCP is a system of equal charges immersed in a static uniform neutralizing background charge. In a Penning trap or Paul trap the applied electromagnetic fields play the role of the uniform background, and one can show that the static thermal equilibrium properties of charges trapped in these systems are the same as those of the OCP (to a differing degree of approximation depending on the trap geometry employed).

The OCP is a paradigm of condensed matter which has been studied for a century [11]. Its properties are directly relevant to the theory of white and brown dwarf interiors, and neutron star crusts [12]. However, experimental data for the dynamical properties of the classical OCP are limited

(although large-scale numerical simulations of the infinite homogeneous OCP have been performed) [13]. Our results point to the possibility that mode experiments on relatively small clouds of trapped ions might be used to experimentally determine dynamical properties of the OCP which are of importance to a range of physical systems.

We examine the frequency and damping of several low-order modes as a function of the shape and size of the plasma cloud as well as the correlation parameter Γ . We also consider the dependence of the modes on the applied magnetic field by examining two limits in our simulations: the unmagnetized case, and the strongly magnetized limit where guiding center equations of motion are valid. Using the aforementioned hydrodynamic model, the frequency shift and damping are employed to extract dynamic properties of the OCP from the simulation data. In particular, we obtain high-frequency bulk and shear moduli, κ and μ , for a range of Γ values and for strongly magnetized as well as unmagnetized systems. The real parts of these moduli, along with the bulk equilibrium plasma pressure, explain the frequency shifts, and the imaginary parts of the moduli describe the damping. In the limit of large Γ the extracted values for κ and μ agree with recent theoretical κ and μ values of an amorphous solid OCP [14].

In simulations of modes in unmagnetized correlated plasmas a number of torsional eigenmodes are also observed. These eigenmodes are shear modes that do not perturb the shape or density of the plasma, so the restoring force for these modes is due only to correlations (i.e., the finite shear modulus μ of the correlated plasma). For the special case of a spherical uniform plasma some theoretical results for such modes are available in the literature on elastic deformations of solid bodies [15,16], and we compare our simulations of the torsional modes to this work.

In Sec. II we review the equilibrium properties of a trapped non-neutral plasma. In Sec. III A the cold-fluid theory of the normal modes of the plasma is reviewed, with particular emphasis on the unmagnetized and guiding center limits. In Sec. III B the predictions of the cold-fluid theory are compared to the results of MD simulations of unmagnetized and guiding center plasmas. The differences between the simulated modes and the cold-fluid theory are described, and compared to a perturbation theory based on the aforementioned viscoelastic approximation, where frequency shifts and damping due to bulk correlation pressure and bulk and shear moduli are predicted. Section IV describes the torsional modes of the unmagnetized plasma, and in Sec. V we discuss some outstanding questions. In Appendix A we review the theory of spheroidal multipole moments, useful in the diagnosis of the modes in our simulations. In Appendix B we work out some special cases of normal modes in crystallized plasmas that can be determined without approximations.

II. EQUILIBRIUM PROPERTIES

In this section we briefly review the static thermal equilibrium properties of a single-species plasma trapped in the applied fields of either a Paul or Penning trap. A more detailed account can be found in Ref. [10]. In a Paul trap [17], charges are confined by the rf fields that result from rapidly

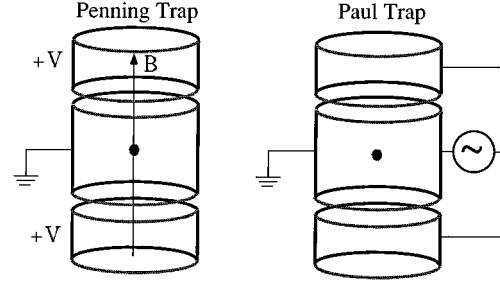


FIG. 1. Diagram of Penning and Paul traps. The traps are shown with cylindrical electrodes, but more complex electrode geometries are often employed. The plasma is the black dot in the trap center, situated within the region where the trap field is harmonic.

oscillating voltages applied to a set of electrodes (Fig. 1). The charges respond to the applied field with a small-amplitude rf jitter motion. This fast jitter in a spatially inhomogeneous rf field produces an average ponderomotive force described by a time-independent effective potential $\phi_e(\mathbf{x})$. In a harmonic trap, this potential is a quadratic function of position over a region around the center of the trap which is sufficiently large to encompass the plasma. We write this potential as

$$\phi_e(\mathbf{x}) = \frac{1}{2} M \omega_z^2 (z^2 + \beta \rho^2), \quad (2.1)$$

where cylindrical coordinates $\mathbf{x} = (\rho, \theta, z)$ are aligned with the trap axis, and \mathbf{x} is measured from the center of the trap. Here ω_z is the axial frequency of a single particle confined in the trap, and the positive constant β is referred to as the trap parameter. (Note that ω_z must be substantially less than the frequency of the applied rf field.) The parameter β can usually be experimentally adjusted, and it determines the symmetry of the confined equilibrium plasma. For example, for $\beta=1$ the plasma will be spherical, whereas for large β the plasma is squeezed radially, becoming a thin elongated spheroid, and for small β the plasma is a flattened pancake.

In a Penning trap [18] (Fig. 1), confinement is provided by static electric and magnetic fields. In a harmonic trap, the electrostatic trap potential satisfies Laplace's equation and is a quadratic function of position

$$\phi_T(\mathbf{x}) = \frac{1}{2} M \omega_z^2 (z^2 - \frac{1}{2} \rho^2).$$

This potential is only confining in the z direction, so a uniform magnetic field is applied in this direction to provide radial confinement. The plasma rotates through the magnetic field about the z axis, causing a $\mathbf{v} \times \mathbf{B}$ force which balances the centrifugal force and the electrostatic repulsion, trapping the plasma radially. In thermal equilibrium the plasma rotates as a rigid body, described by a constant rotation frequency ω_r about the trap axis. The confining $\mathbf{v} \times \mathbf{B}$ force and the centrifugal force are then proportional to radius ρ , and in the rotating frame they appear in the equations of motion as the derivative of a pseudopotential proportional to ρ^2 . Thus in the rotating frame the charges experience a static effective confinement potential $\phi_e(\mathbf{x})$ equal to the sum of the pseudopotential and $q\phi_T$ [19]. This effective potential is quadratic

in z and ρ , and so is of the same form as Eq. (2.1). Now the trap parameter β is related to the rotation frequency

$$\beta = \frac{-\omega_r(\Omega_c + \omega_r)}{\omega_z^2} - \frac{1}{2}, \quad (2.2)$$

and $\omega_r, \Omega_c < 0$ is required for confinement (electrons rotate counterclockwise, positive ions clockwise when observed from the positive z axis). Thus the plasma in the Penning trap has the same thermal equilibrium properties in the rotating frame as the plasma in the Paul trap. Throughout this paper we consider properties of plasmas in Penning traps as observed in the rotating frame.

The thermal equilibrium properties of low-temperature single species plasmas confined in the harmonic trap potential in Eq. (2.1) have been discussed extensively in previous papers [20,21]. If one neglects correlations, the zero-temperature thermal equilibrium state has been shown to be a uniform-density spheroid (ellipsoid of revolution). The density n_0 is related to the external confining fields

$$n_0 = \frac{M\omega_z^2}{4\pi q^2}(2\beta + 1), \quad (2.3)$$

and the aspect ratio α of the plasma spheroid is related to the trap parameter

$$2\beta + 1 = \frac{\alpha^2 - 1}{Q_1^0(\alpha/\sqrt{\alpha^2 - 1})}, \quad (2.4)$$

where Q_1^0 is a Legendre function of the second kind. [This equation is equivalent to Eq. (2.6) of Ref. [10].] The aspect ratio is defined as $\alpha = L/R$, where $2R$ is the diameter of the spheroid and $2L$ is its length. When one specifies the total number of charges N , the length and radius are then determined by the shape and volume of the spheroid: $\frac{4}{3}\pi LR^2 n_0 = N$, and this relation can be written in terms of the aspect ratio α and the Wigner-Seitz radius a_{WS} , reproduced here from Ref. [10] for convenience:

$$\left(\frac{L}{a_{\text{WS}}}\right)^3 = N\alpha^2, \quad \left(\frac{R}{a_{\text{WS}}}\right)^3 = \frac{N}{\alpha}. \quad (2.5)$$

Equations (2.2)–(2.5) have been verified experimentally in Penning trap experiments [21].

Up to this point we have not discussed correlations. We now briefly review the effect of interparticle correlations on the plasma equilibrium. When the correlation parameter Γ is larger than unity, the interparticle correlations increasingly favor the establishment of order within the plasma.

The thermal equilibrium properties of the strongly correlated infinite homogeneous OCP have been determined theoretically through a combination of analytic and numerical techniques. The system is predicted to exhibit short-range order characteristic of a liquid for $\Gamma \gtrsim 2$ [11], and a first-order phase transition to a body-centered-cubic (bcc) lattice at $\Gamma \approx 172$ [22,23]. Useful relations between the thermodynamic functions have also been found. In particular, the bulk pressure p of the OCP is related to the correlation contribution to the internal energy U through

$$p = n_0 kT \left(1 + \frac{1}{3} \frac{U}{NkT}\right), \quad (2.6)$$

and furthermore U/NkT is a function only of Γ . The form for U/NkT in the liquid phase has been determined from Monte Carlo simulations [24] and in the solid phase from a combination of analytic and numerical techniques [22]. At small Γ , U/NkT approaches zero. At large Γ in the crystalline phase U/NkT is proportional to Γ , $U/NkT \rightarrow A\Gamma$, where the Madelung constant $A \approx -0.90$ for several stable lattice types including bcc, fcc, and hcp.

However, in the trapped clouds of interest here, the correlation properties are different than those of the infinite OCP due to surface effects. In particular, the density is no longer uniform, and this affects the correlations. For small values of Γ the plasma density falls monotonically to zero at the plasma edge on the scale of a Debye length [25]. As the temperature decreases, the Debye length decreases and the plasma edge steepens, approaching the uniform density of cold-fluid theory. However, as Γ increases beyond around $\Gamma \sim 2$ the density also begins to exhibit spatially decaying oscillations from the outer edge inward with a wavelength on the order of a_{WS} [23] (see, for example, Fig. 1 of Ref. [10]). As Γ increases further the oscillations increase in magnitude until finally the density approaches zero between the peaks and the system forms a number of concentric shells [1,2]. These shells may be thought of as lattice planes which are curved to satisfy the boundary conditions imposed by the external potential into a roughly spheroidal shape. At intermediate values of Γ ($\Gamma \sim 100$), charges diffuse within these shells, but rarely hop between them; whereas at large Γ values ($\Gamma \gtrsim 300$ – 1000) the charges generally crystallize into a distorted two-dimensional (2D) hexagonal structure, although for extremely oblate or prolate clouds other crystal structures can occur [26]. Although correlations in the trapped plasma are quite different than those of the infinite OCP, we will observe in Sec. III that their effect on the collective modes of the trapped plasma can be explained by reference to bulk correlation properties of a homogeneous OCP.

III. NORMAL MODES

In this section we discuss the behavior of low-order normal modes of oscillation of a strongly correlated plasma in a harmonic trap. We compare a recent cold-fluid theory for the modes to the results of molecular-dynamics simulations of oscillations in low-temperature ion clouds. We first discuss the cold-fluid theory for the modes. This theory neglects correlation effects and treats the plasma as a cold uniform fluid. A more detailed review of the theory can be found in Ref. [10]. Differences between the cold-fluid theory and computer simulations of the modes in a strongly correlated plasma will be considered in Sec. III B.

A. Cold-fluid theory

The normal modes of a plasma spheroid have recently been enumerated [7]. This is the only known analytic solution for modes of a realistic three-dimensionally confined magnetized plasma. Here we will focus on the two limiting

cases of very strong magnetic fields where the vortex frequency [27] $\Omega_v = \Omega_c + 2\omega_r$ is large compared to the plasma frequency, and weak magnetic fields, where $|\Omega_v| \rightarrow 0$. The vortex frequency is the cyclotron frequency as seen in a frame rotating with the plasma; the $2\omega_r$ frequency shift arises from the Coriolis force, which acts like a uniform magnetic field in the rotating frame. Since Paul trap plasmas are unmagnetized and almost always have negligible rotation frequency, they fall in the unmagnetized regime $\Omega_v = 0$, whereas Penning trap plasmas can span the range between unmagnetized and strongly magnetized limits, depending on the values of ω_r/Ω_c and ω_z/Ω_c . In particular, at the Brillouin limit [28] $|\omega_r/\Omega_c| = \frac{1}{2}$, the vortex frequency vanishes, and in the rotating frame the plasma is unmagnetized, whereas away from this limit a range of ω_r/Ω_c values exists for which the plasma becomes strongly magnetized provided that $\Omega_c/\omega_z \gg 1$ [this follows from Eqs. (2.2) and (2.3) and the definition of Ω_v].

In cold-fluid theory, the normal modes are described by the perturbed potential $\psi(\mathbf{x}, t)$ induced by the mode, as seen in a frame rotating with the plasma at frequency ω_r . In the rotating frame $\psi(\mathbf{x}, t)$ is assumed to vary with time as $\exp(-i\omega t)$. This assumption leads to the following differential equation for ψ [7,10]:

$$\nabla \cdot (\boldsymbol{\varepsilon} \cdot \nabla \psi) = 0, \quad (3.1a)$$

with the boundary condition $\psi \rightarrow 0$ as $|\mathbf{x}| \rightarrow \infty$ (image charges are neglected since the plasma is assumed small compared to the trap electrodes). The tensor $\boldsymbol{\varepsilon}$ is the cold-fluid dielectric tensor. Outside the plasma $\boldsymbol{\varepsilon} = 1$, whereas inside the plasma

$$\boldsymbol{\varepsilon} = \begin{pmatrix} \varepsilon_1 & -i\varepsilon_2 & 0 \\ i\varepsilon_2 & \varepsilon_1 & 0 \\ 0 & 0 & \varepsilon_3 \end{pmatrix} \quad (3.1b)$$

in Cartesian coordinates. The dielectric coefficients ε_1 , ε_2 , and ε_3 depend on the frequency ω of the mode, as well as the plasma and vortex frequencies:

$$\begin{aligned} \varepsilon_1 &= 1 - \omega_p^2/(\omega^2 - \Omega_v^2), & \varepsilon_2 &= \omega_p^2 \Omega_v / \omega(\omega^2 - \Omega_v^2), \\ \varepsilon_3 &= 1 - \omega_p^2/\omega^2, \end{aligned} \quad (3.1c)$$

where $\omega_p = \sqrt{4\pi q^2 n_0 / M}$ is the plasma frequency.

In the unmagnetized limit the vortex frequency Ω_v vanishes, the dielectric tensor $\boldsymbol{\varepsilon}$ is isotropic, and Eq. (3.1a) can be solved in spheroidal coordinates. However, when Ω_v is nonzero the solution is not as straightforward; nevertheless a separable solution can still be obtained. For the purposes of this paper we will have need only of the solution interior to the plasma, ψ^{in} , which separates in scaled spheroidal coordinates [7]. The interior mode potential ψ^{in} also has a relatively straightforward (though nonseparable) polynomial form in cylindrical coordinates, which we will find useful when we diagnose our mode simulations. In Table I of Ref. [10] we provide the cylindrical forms for several of the low-order modes. Modes are parametrized by two quantum numbers l and m , $l \geq 1$ and $|m| \leq l$. These numbers determine the degree of variation of the mode potential; $|m|$ equals the number of zeros in the potential as one circles the equator of the

spheroid, and $l - |m|$ equals the number of zeros one encounters upon traversing a great circle from pole to pole.

1. Unmagnetized modes

In the unmagnetized limit $\Omega_v = 0$ the modes become surface plasma oscillations on a spheroid. These unmagnetized surface plasma oscillations are incompressible deformations of the shape of the spheroid. In the spherical limit $\alpha = 1$ the surface mode frequencies are given by

$$\omega^2 = \frac{\omega_p^2 l}{2l + 1} \quad (3.2)$$

[see Eq. (3.8) of Ref. [10]].

In addition to the surface modes, there is also a set of unmagnetized bulk plasma modes for which $\omega^2 = \omega_p^2$ [7,10]. These bulk modes cause potential perturbations within the plasma which do not affect the external potential; that is, $\psi^{\text{out}} = 0$ for these modes. For example, in a spherical plasma a density perturbation that is any function of spherical radius r oscillates at the plasma frequency. In particular, there is a bulk plasma mode in a spherical unmagnetized plasma for which the perturbed interior potential is quadratic in r : $\psi^{\text{in}} = A(r^2 - R^2)$. This mode corresponds to breathing oscillations of the sphere [see Fig. 2(e)]. Such breathing modes also occur for more general plasma equilibria, such as spheroidal, cylindrical, or disc plasmas. For the particular cases of spherical, cylindrical, and disc plasmas, the breathing mode also happens to be an exact crystal eigenmode (see Appendix B). Simulations of the breathing mode will be discussed in Sec. III B 7.

Looking ahead for a moment, we note that there is another class of modes in unmagnetized plasmas that does not exist in the cold-fluid theory discussed here. These are the torsional modes, which are twisting oscillations that do not affect the shape or density of the plasma. An example of such a mode is shown in Fig. 2(f). The restoring force for these modes arises entirely from correlation effects (i.e., the shear modulus of the plasma). Such correlation effects do not exist in cold-fluid theory. These modes occur only for unmagnetized plasmas. In the presence of a magnetic field the Lorentz force dominates over the shear force, and the modes change character. We will return to this point in Sec. III A 2 when we consider magnetized plasma modes. We discuss simulations of unmagnetized torsional modes in Sec. IV.

2. Modes in a strong magnetic field

For a spheroidal plasma in a magnetic field the mode frequencies are determined by Eq. (3.11) of Ref. [10]. When the magnetic field is large the frequencies fall into three regimes. The highest frequency modes are upper hybrid oscillations with frequencies near Ω_p . These modes consist of rapid oscillations predominantly across the magnetic field. The next set of modes are magnetized plasma oscillations with frequencies of order ω_p or less. These modes consist of plasma motions mainly along the direction of magnetic field. Finally, there are low frequency $\mathbf{E} \times \mathbf{B}$ drift modes with frequencies of $O(\omega_p^2/\Omega_c)$. These modes consist of slow drift motions mainly across the magnetic field.

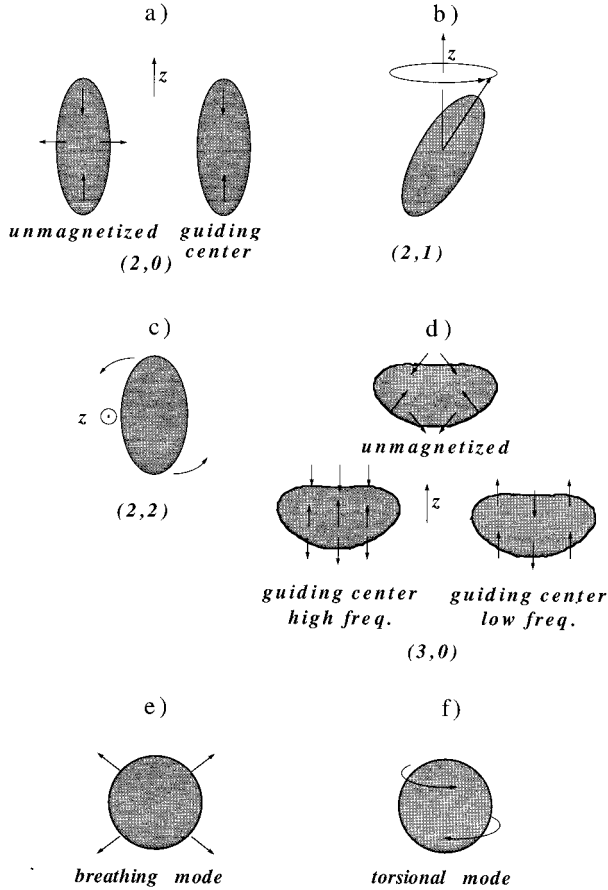


FIG. 2. Deformations of the plasma due to normal modes of various types. The arrows indicate the direction of motion. (a) (2,0) mode: spheroid oscillates in radius and/or length. (b) (2,1) mode: spheroid tilts and precesses around the trap axis. (c) (2,2) mode: spheroid deforms into triaxial ellipsoid, and rotates around the trap axis. (d) (3,0) mode: in the large Ω_v limit, two types of magnetized plasma modes exist. In the unmagnetized limit, the single (3,0) surface mode is incompressible. (e) Breathing mode: sphere expands and contracts in radius. (f) Example of a torsional mode: top half of sphere twists with respect to bottom half.

For given values of l and m there is a finite number of magnetized modes. For $m=0$ there are $2l$ modes. For $m \neq 0$ and $l-m$ even there are $2(l-|m|)+2$ modes, while for $m \neq 0$ and $l-m$ odd there are $2(l-|m|)+1$ modes.

As $\Omega_v \rightarrow 0$ the magnetized modes connect to the unmagnetized modes in the following manner: if $m=0$ all upper hybrid modes become degenerate bulk plasma oscillations, and two of the magnetized plasma modes become the surface plasma oscillations. The rest of the modes approach zero frequency. (Actually, when correlation effects are taken into account these zero-frequency modes become torsional oscillations.) If $m \neq 0$ the same thing happens as $\Omega_v \rightarrow 0$, except that now only one of either the magnetized plasma or $\mathbf{E} \times \mathbf{B}$ modes becomes a surface plasma mode, and an upper hybrid mode also becomes a surface plasma mode.

3. Low-order modes

The low-order modes have straightforward physical interpretations. The (2,0) mode is an oscillation in the aspect ratio

of the spheroid [Fig. 2(a)]. In the limit of strong magnetic field the spheroid contracts and expands along the magnetic field [a plasma mode, shown in Fig. 2(a)] or across the magnetic field (an upper hybrid mode, not shown). In the unmagnetized limit the (2,0) mode is incompressible, and the spheroid radius decreases as the length increases. For both magnetized and unmagnetized plasma, the (2,1) mode corresponds to an incompressible tilt of the spheroid with respect to the z axis. The tilted plasma precesses around the z axis at the mode frequency [see Fig. 2(b)]. The (2,2) mode is also incompressible, corresponding to a deformation of the plasma into a triaxial ellipsoid with a major axis parallel to z [see Fig. 2(c)]. The ellipsoid then rotates about the z axis. For the (3,0) mode, there are two different types of magnetized plasma oscillation in the magnetized case, shown in Fig. 2(d). There is also an upper hybrid oscillation (not shown). In the unmagnetized limit the single surface plasma oscillation is again incompressible, also shown in Fig. 2(d).

B. Simulations of the normal modes and comparison to fluid theory

We have carried out computer simulations of the normal modes in order to test the cold-fluid theory and examine the effect of correlations on the normal modes. Two separate molecular-dynamics algorithms were employed in this effort in order to study both magnetized and unmagnetized dynamics. One code followed unmagnetized charged particle trajectories in the effective trap potential given by Eq. (2.1) [1], and the other employed guiding center equations to follow the motion of charges in a Penning trap in the guiding center limit [2], averaging over the fast cyclotron motion. Because cyclotron motion is averaged out in the second code, the guiding centers are described by only four variables, position \mathbf{x} and the z component of velocity v_z . The other two components of the velocity are determined by the $\mathbf{E} \times \mathbf{B}$ drift velocity of the guiding center. Upper hybrid modes cannot be simulated with this code: only plasma and $\mathbf{E} \times \mathbf{B}$ modes can be followed. However, both magnetized and unmagnetized codes are similar in that they follow the trajectories of N charges under the influence of the external fields as well as the Coulomb interactions with the other charges.

1. Initial preparation of the system

Simulations of the modes were carried out in the following manner. Initial conditions were generated using a simulated plasma which was previously allowed to equilibrate. For simulations of crystallized ($\Gamma \rightarrow \infty$) plasmas this involved slowly cooling the system by extracting kinetic energy until a potential energy minimum was obtained. For large N there are many nearly identical local energy minima. In some cases great care was taken to obtain a minimum energy as close as possible to the global minimum by cooling very slowly and then annealing the crystal by reheating and recooling several times. In other cases no attempt was made to anneal the crystal to a better minimum, but there was negligible difference in the mode frequencies between these cases.

For simulations of modes in finite Γ plasmas, the equilibrium was set up in a different manner. In the guiding center simulations a given Γ value was arrived at by employing the

TABLE I. Frequencies of (2,0) modes in spherical guiding center and unmagnetized plasmas.

	$\omega_{\text{simulation}}/\omega_z$	$\omega_{\text{theory}}/\omega_z$
$B=0$	1.0955	$\sqrt{6/5}=1.0954 \dots$
Guiding center	1.3418	$3/\sqrt{5}=1.3416 \dots$

Metropolis-Rosenbluth Monte Carlo method to obtain realizations of the charge positions at a given Γ value. The particles were then given a random distribution of kinetic energies with a mean corresponding to this value of Γ . The system was then integrated forward in time via guiding center molecular dynamics for several hundred plasma periods to allow full equilibration. In the unmagnetized simulations the system was prepared at a given Γ value by introducing random components of velocity in the MD code and then allowing the system to interact and equilibrate in a heat bath (rescaling each velocity component so as to ensure that the average kinetic energy remains at a certain level, and using a canonical touch periodically to randomize velocities of a fraction of the particles in order to follow the appropriate Boltzmann distribution).

2. Addition of a mode perturbation

In order to set up a normal mode of oscillation in both types of simulations, we extracted positions $\mathbf{x}_i^{(0)}$ and velocities $\mathbf{v}_i^{(0)}$, $i=1, \dots, N$, of the equilibrated charges at some time step. To these positions and velocities we added a perturbation associated with a given fluid normal mode, according to Eq. (3.1b) of Ref. [10],

$$\mathbf{x}_i(t=0) = \mathbf{x}_i^{(0)} + \text{Re}[\delta\mathbf{x}_i], \quad (3.3a)$$

$$\mathbf{v}_i(t=0) = \mathbf{v}_i^{(0)} + \text{Re}[\delta\mathbf{v}_i], \quad (3.3b)$$

$$\delta\mathbf{v}_i = -\frac{\sigma}{qn_0} \cdot \nabla \psi^{\text{in}}(\mathbf{x}_i^{(0)}), \quad (3.3c)$$

and

$$\delta\mathbf{x}_i = -\delta\mathbf{v}_i/i\omega, \quad (3.3d)$$

where σ is the cold-fluid conductivity tensor,

$$\sigma = \frac{\omega}{4\pi i}(\varepsilon - 1). \quad (3.3e)$$

Only the z component of Eq. (3.3b) is required for the guiding center simulations. For example, in the guiding center limit $\Omega_v \rightarrow \infty$, one finds the displacements associated with a (2,0) mode by taking ψ_{in} from Table I of Ref. [10] and applying it to Eqs. (3.3), using Eq. (3.1b) for ε . This procedure yields the initial condition

$$\mathbf{x}_i(t=0) = \mathbf{x}_i^{(0)}, \quad v_{z_i}(t=0) = v_{z_i}^{(0)} + C_{z_i}^{(0)} \quad (3.4a)$$

for some amplitude C . For the unmagnetized ($\Omega_v = 0$) (2,0) mode the same equations imply

$$\mathbf{x}_i(t=0) = \mathbf{x}_i^{(0)},$$

$$\mathbf{v}_i(t=0) = \mathbf{v}_i^{(0)} + C(-x_i^{(0)}/2, -y_i^{(0)}/2, -z_i^{(0)}). \quad (3.4b)$$

The perturbation amplitude C was chosen to be sufficiently small to be linear. The condition of linearity can be couched in the form $|\nabla \delta\mathbf{x}| \ll 1$, or, in other words, the maximum value of $|\delta\mathbf{x}|$ must be small compared to the mode wavelength, of order $a_{\text{WS}}N^{1/3}$ for a low-order mode.

On the other hand, the amplitude must be chosen to be larger than the thermal fluctuations, otherwise the mode cannot be observed over the thermal noise. The kinetic energy fluctuates by an amount of order $\sqrt{N}kT$, and the mode kinetic energy is of order $NM\delta v^2 = NM\omega^2\delta x^2$, so for N sufficiently large or T sufficiently small the modes can be observed above the noise even when the modes are in the linear regime: $\sqrt{kT/(m\omega^2N^{1/2})} \ll |\delta\mathbf{x}| \ll a_{\text{WS}}N^{1/3}$. For example, for the (2,0) mode this condition implies $(\omega_p/\omega)/(\sqrt{3}\Gamma N^{7/12}) \ll C/\omega \ll 1$, a condition that is easily met for large Γ and large N .

From these initial conditions the plasma was then allowed to freely evolve without additional external perturbations (total energy and component of angular momentum along the trap are conserved, and the center of mass position remains fixed at the trap center). In the unmagnetized code time steps were chosen to equal $2\pi/100$ times the one-particle period. In the guiding center simulation time steps were allowed to vary in size in order to conserve energy at a level of roughly $10^{-5}q^2/a_{\text{WS}}$ for each time step. The system was then followed for several hundred single-particle periods. The numerical accuracy of the simulations was checked at several points by repeating some simulations with different constraints on the energy conservation (guiding center case) and with different sized time steps (unmagnetized case).

In the guiding center simulations the magnetic field was chosen differently for different modes. For the (2,0) and (3,0) modes $\Omega_c/\omega_z = 10$, for the (2,1) mode $\Omega_c/\omega_z = 10^5$, and for the (2,2) mode $\Omega_c/\omega_z = 10/3$. The magnetic field was chosen to be relatively large for the (2,1) mode simulations in order to make degenerate the two plasma modes with opposite signs of ω/m (opposite phase velocities), since at finite Ω_c these two (2,1) modes occur at two separate frequencies. For the (2,2) mode the magnetic field was chosen to be relatively small because the guiding center (2,2) frequency scales as ω_p^2/Ω_c , and so a frequency measurement of the (2,2) mode is difficult if Ω_c is too large. However, since guiding center equations of motion are used in the molecular-dynamics simulation the guiding center limit of the cold-fluid dispersion relation, Eqs. (3.11) and (3.12) of Ref. [10], is still applicable even when Ω_c is not large.

3. Extraction of multipole moments and mode frequencies

The oscillations of the plasma resulting from the above-described initial conditions were diagnosed by taking multipole moments of the density as a function of time. If the multipole moments are defined properly—that is, if they are chosen to be spheroidal multipole moments rather than the more common spherical multipoles—one can show that an oscillation having given mode numbers l and m excites only a single spheroidal multipole moment $q_{lm}(t)$, independent of

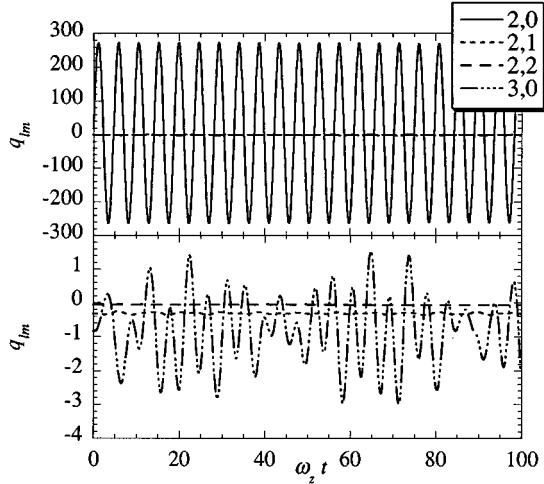


FIG. 3. Multipole moments $q_{lm}(t)$ of an initially spherical crystallized cloud of $N=1000$ charges with a $(2,0)$ perturbation added with magnitude $C=0.03\omega_z$, following guiding center dynamics [see Eq. (3.4a)]. The lower plot shows a blowup of the upper plot in order to display the moments with $(l,m) \neq (2,0)$, which have much lower amplitude than the $(2,0)$ moment. For $m \neq 0$ only the real parts of the moments are displayed. Moments are normalized to the Wigner-Seitz radius a_{WS} .

the strength of the magnetic field. A review of spheroidal multipole moments is provided in Appendix A. Like spherical multipoles, these spheroidal multipoles can be written as sums over polynomial density moments. For example,

$$q_{20}(t) = \frac{1}{3} \sqrt{5/\pi} \int d^3x n(\mathbf{x},t) \left\{ \frac{3}{4} (2z^2 - \rho^2) - \frac{3}{10} d^2 \right\}$$

$$= \frac{1}{3} \sqrt{5/\pi} \sum_{i=1}^N \left\{ \frac{3}{4} [2z_i^2(t) - \rho_i^2(t)] - \frac{3}{10} d^2 \right\},$$

where $d^2 = L^2 - R^2$. [In this form for q_{20} we have subtracted out the contribution to the quadrupole moment of the spheroidal equilibrium, so that q_{20} oscillates around zero in the simulations of the $(2,0)$ mode.] The form of q_{lm} for general l and m is given in Appendix A.

An example of this diagnostic is shown in Fig. 3, which displays several multipole moments for an initially spherical crystallized cloud of 1000 charges to which a $(2,0)$ perturbation has been added using Eq. (3.4a). The guiding center limit of the dynamics has been employed. The figure shows that the $(2,0)$ multipole is excited and oscillates sinusoidally, whereas other multipole moments are smaller by roughly two orders of magnitude.

The mode frequency can be extracted by making a sinusoidal fit to the oscillation of q_{20} shown in the figure. The result of the fit is displayed in Table I and compared to the fluid theory, Eq. (3.11) in Ref. [10]. The agreement is excellent. The table also shows a similar level of agreement with the fluid theory [Eq. (3.2)] when an unmagnetized $(2,0)$ mode is simulated using the same initial plasma.

In Fig. 4(a) we display how the $(2,0)$ frequency varies for crystallized plasmas of different shapes. Excellent agreement between the fluid theory and the simulations is observed for both magnetized and unmagnetized dynamics. In Figs. 4(b)–

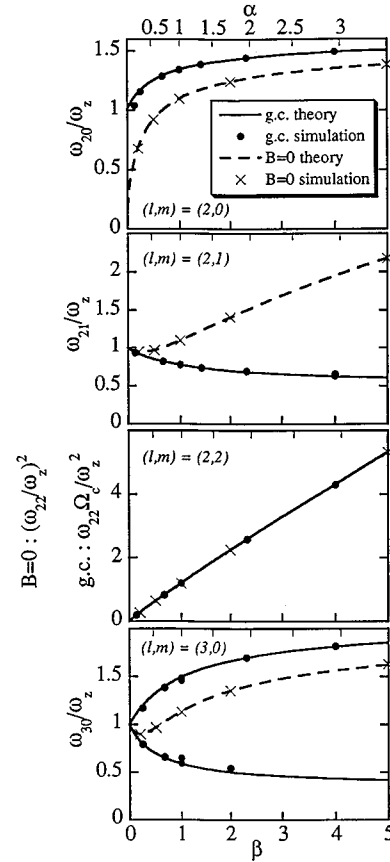


FIG. 4. Mode frequencies for crystallized plasmas as a function of plasma shape for different low-order modes. Dots are simulation results for guiding center modes, crosses for unmagnetized modes. The solid line is the cold-fluid theory for guiding center plasmas [Eqs. (3.11) and (3.12) of Ref. [10]], and dotted line is the theory for unmagnetized plasmas [Eq. (3.7) of Ref. [10]]. Frequencies are normalized to the axial bounce frequency ω_z , except for the $(2,2)$ $\mathbf{E} \times \mathbf{B}$ mode, which is normalized to ω_z^2/Ω_c^2 , where Ω_c is the cyclotron frequency. Note that the guiding center $(2,2)$ frequency, when normalized in this manner, equals the square of the unmagnetized $(2,2)$ frequency normalized to ω_z (Ref. [10]). There are two guiding center $(3,0)$ modes (see Fig. 2). (a) $(2,0)$ mode. (b) $(2,1)$ mode. (c) $(2,2)$ mode. (d) $(3,0)$ mode.

4(d) the frequency of modes set up in crystallized plasmas for other values of l and m is also compared to the fluid theory, and in each case very good agreement is obtained for the mode frequency. Note that ω^2/ω_z^2 for an unmagnetized $(2,2)$ mode is predicted to be the same function of β as is $\omega\Omega_c/\omega_z^2$ for the guiding center $(2,2)$ mode [10], and this prediction is verified in the simulations.

4. Frequency deviations from the cold-fluid theory

However, there are small differences between the fluid theory and the simulations. There is a small but systematic shift in the simulated mode frequencies which is difficult to see in Figs. 4. For various values of the trap parameter β the difference $\Delta\omega = \omega_{\text{sim}} - \omega_{\text{fluid}}$ between the simulated mode frequency ω_{sim} and the cold-fluid theory ω_{fluid} is displayed in Fig. 5. We evaluate the frequency shifts of the $(2,0)$, $(2,1)$, $(2,2)$, and $(3,0)$ unmagnetized surface plasma modes as well

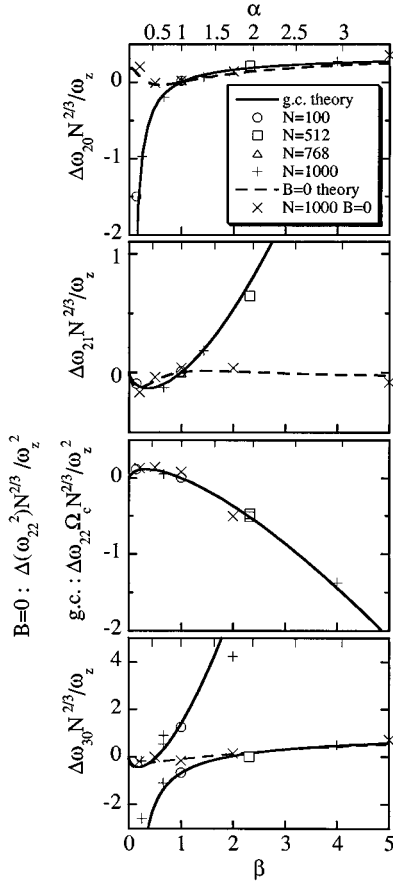


FIG. 5. Difference between mode frequencies as observed in simulations of crystallized ($\Gamma \rightarrow \infty$) ion clouds and the cold-fluid theory, $\Delta\omega = \omega_{\text{sim}} - \omega_{\text{fluid}}$. Frequency differences are plotted as a function of trap parameter β on the lower x axis, and plasma aspect ratio α on the upper x axis. α is determined from β via the cold-fluid relation, Eq. (2.4). (a) (2,0) mode shift. (b) (2,1) mode. (c) (2,2) mode. (d) (3,0) mode. Solid lines are the theory predictions for the frequency shifts in the guiding center limit, dashed lines are predicted shifts for $B=0$. For the (2,2) modes the predicted frequency shifts for these two cases coincide when normalized as shown in the figure.

as their guiding center counterparts for clouds which are crystallized ($\Gamma \rightarrow \infty$). The frequency shifts are scaled by $N^{2/3}$ in order to make contact with a theory for the shifts discussed below. For the $l=2$ modes the shifts appear to vanish for spherical plasmas, hence the excellent agreement between the fluid theory and the simulations observed in Table I.

The frequency shift is also found to depend on the cloud temperature. For example, for a spherical cloud there is a negligible frequency shift of the guiding center (2,0) mode at large Γ [see Fig. 5(a) and Table I]. However, as temperature is increased, a positive shift in frequency appears (see Fig. 6). For an unmagnetized plasma the frequency shift is smaller as temperature varies (Fig. 6).

In Ref. [10] it was predicted that such frequency shifts arise through two effects which are neglected in cold-fluid theory. First, plasma pressure changes the equilibrium shape and density of the plasma, which in turn changes the mode

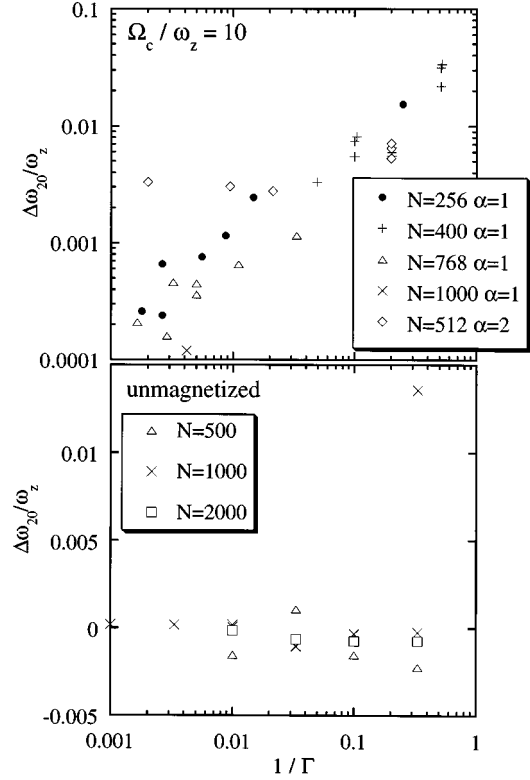


FIG. 6. Frequency shift $\Delta\omega_{20}$ of the (2,0) normal mode from the fluid result in spherical ($\alpha=1$) and prolate ($\alpha=2$) clouds of various sizes as a function of the inverse correlation parameter, $1/\Gamma$. The upper plot is for a guiding center simulation with $\Omega_c/\omega_z=10$, where Ω_c is the cyclotron frequency and ω_z the axial bounce frequency. The lower plot is for an unmagnetized spherical plasma.

frequencies. Second, extra restoring forces appear due to the elastic properties of the strongly correlated system; these are described by isotropic bulk and shear moduli κ and μ . The following expressions for the frequency shifts $\Delta\omega$ were derived using this elastic model of the plasma, assuming that shifts were small, the plasma was strongly correlated, and the modes in question were not degenerate.

For the (1,0) and (1,1) modes $\Delta\omega=0$, as befits these center of mass oscillations. For the (2,0), (2,1), (2,2), and (3,0) surface modes in an unmagnetized plasma the following predictions were derived for the frequency shifts:

$$\Delta\omega = \frac{15\omega}{R^2 + 2L^2} \frac{p + \mu\omega_p^2/\omega^2}{M\omega_p^2 n_0} \quad \text{for } (l,m)=(2,0), \quad (3.5a)$$

$$\Delta\omega = \frac{10\omega}{(L^2 + R^2)} \frac{p + \mu\omega_p^2/\omega^2}{M\omega_p^2 n_0} \quad \text{for } (l,m)=(2,1), \quad (3.5b)$$

$$\Delta\omega = \frac{5\omega}{R^2} \frac{p + \mu\omega_p^2/\omega^2}{M\omega_p^2 n_0} \quad \text{for } (l,m)=(2,2), \quad (3.5c)$$

$$\Delta\omega = \frac{70\omega(3L^2 + 2R^2)}{(2L^2 + 3R^2)(4L^2 + R^2)} \frac{p + \mu\omega_p^2/\omega^2}{M\omega_p^2 n_0}$$

for $(l, m) = (3, 0)$, (3.5d)

where ω is the frequency of the given unmagnetized cold-fluid mode as seen in the rotating frame. The bulk modulus κ does not appear in these expressions because the unmag-

netized surface modes induce incompressible deformations of the plasma shape in fluid theory, so only the shear modulus μ appears, describing the elastic response to shear of the correlated plasma. The bulk pressure p [Eq. (2.6)] also appears, describing the effect on the modes of the change in the equilibrium shape and density when pressure is taken into account.

In the guiding center limit similar expressions were derived:

$$\Delta\omega = \frac{5\omega}{2L^2} \frac{2p\varepsilon_3 + (\kappa + 4\mu/3)\omega_p^2/\omega^2}{M\omega_p^2 n_0} \quad \text{for } (l, m) = (2, 0), \quad (3.6a)$$

$$\Delta\omega = \frac{5\omega}{2R^2} \frac{2p + \mu\omega_p^2/\omega^2}{M\omega_p^2 n_0} \quad \text{for } (l, m) = (2, 1), \quad (3.6b)$$

$$\Delta\omega = \frac{10\omega}{R^2} \frac{p + \mu\omega_p^2/\omega\Omega_c}{M\omega_p^2 n_0} \quad \text{for } (l, m) = (2, 2), \quad (3.6c)$$

$$\Delta\omega = 35\omega \frac{2L^2[2p\varepsilon_3 + (\kappa + 4\mu/3)\omega_p^2/\omega^2] + (R\varepsilon_3)^2[2p + \mu\omega_p^2/\omega^2]}{M\omega_p^2 n_0 [8L^4 + 4R^2L^2\varepsilon_3 + 3R^4\varepsilon_3^2]} \quad \text{for } (l, m) = (3, 0). \quad (3.6d)$$

Equations (3.6) neglect a magnetic field effect discussed in Ref. [10]: for $B \neq 0$ there are more than two moduli, having the effect that the moduli can have different values for different modes. However, for frequency shifts at large Γ this effect is unimportant (see Ref. [10] for details).

For the magnetized (2,0) and (3,0) modes the bulk modulus κ now appears because the modes are no longer incompressible. For the (3,0) guiding center mode there are two possible frequencies of oscillation (see Fig. 4), and the frequency shift depends on which (3,0) frequency one employs in Eq. (3.6d).

All of the frequency shifts are predicted to scale as $1/(\text{plasma size})^2$. This is because the effective wavelength λ of these low-order modes is on the order of the plasma size, and a frequency shift due to pressure effects will be on the order of $p/(mn_0\lambda^2)$. This is the form of the frequency shift in the Bohm-Gross dispersion relation for unmagnetized warm plasma waves in an infinite uncorrelated plasma [29], $\omega^2 = \omega_p^2 + \gamma(kT/m)(2\pi/\lambda)^2$ (where γ is the ratio of specific heats). Since the plasma size scales as $N^{1/3}$, the size of the plasma can be scaled out of the frequency shift by multiplying $\Delta\omega$ by $N^{2/3}$, as in Figs. 5 and 6. The scaled frequency shift $\Delta\omega N^{2/3}/\omega$ depends on the plasma shape α , correlation parameter Γ , the magnetic field strength in the rotating frame scaled by the plasma frequency Ω_v/ω_p , and the particular mode in question.

The qualitative dependence of the frequency shift on plasma shape can also be understood from the idea of an effective wavelength λ for the modes. For example, the shift becomes large and negative in oblate clouds for the guiding center (2,0) mode, and is even larger for the high-frequency guiding center (3,0) mode in the oblate limit. This is because

these modes correspond to compressions and rarefactions of the plasma along the magnetic field (magnetized plasma waves), with a wavelength λ on order of $4L$ for the (2,0) mode and of order $2L$ for the (3,0) mode (see Fig. 2). In both cases, as the plasma becomes oblate λ decreases and the frequency shift becomes more negative (opposite to the Bohm-Gross dispersion relation), because the bulk compressibility $(\kappa + 4/3\mu)$ of the strongly correlated plasma is negative, leading to negative dispersion of plasma waves [13, 14, 30].

In order to make a more detailed comparison of these theoretical predictions for the mode frequency shifts to our computer simulation results, we need expressions for the equilibrium pressure p and the bulk and shear moduli κ and μ for a strongly correlated plasma. While the equilibrium pressure is known for a strongly correlated plasma as a function of Γ [Eq. (2.6)], precise forms for the bulk and shear moduli are not known. In general, these moduli are functions of Γ as well as frequency ω and magnetic field B . Since the oscillations are generally rapid compared to equilibrium times, the high-frequency limits for κ and μ may be sufficient. In the very strongly correlated limit $\Gamma \gg 1$, some results are then available. The dielectric function for a strongly correlated homogeneous isotropic amorphous solid one-component plasma has recently been derived using a two-time-scale approximation [14]. The derivation neglects viscous damping and diffusion, so only the high-frequency elastic response is kept. This dielectric function allows one to extract the real parts of κ and μ by comparing the long-wavelength form of the dielectric function to the dispersion relations for compressional and shear modes in a homogeneous isotropic system with given bulk and shear moduli [31]. The results, valid for $\Gamma \gg 1$, are

$$\kappa + \frac{4}{3}\mu = \frac{4}{15}n_0 \frac{U}{N}, \quad (3.7a)$$

$$\mu = -\frac{2}{15}n_0 \frac{U}{N}, \quad (3.7b)$$

where U/N is the correlation internal energy per particle discussed in Sec. II.

In the limit $\Gamma \rightarrow \infty$, where $U/N \approx -0.90q^2/a_{ws}$, these expressions for the moduli can be used in Eqs. (3.5) and (3.6) to extract predictions for the frequency shifts which can be compared to the simulation results. In Figs. 5 the theoretical predictions for the shifts are shown as the solid curves for guiding center modes and dashed curves for unmagnetized modes. One finds good agreement between the theory and the simulations, with no adjustable parameters. For example, for spherical plasmas the theory predicts no frequency shift for $l=2$ modes, just as is observed in the simulations. The theory begins to fail only when the effective wavelength of the modes becomes comparable to the interparticle spacing. This occurs for the guiding center (2,0) and high-frequency (3,0) modes in very oblate plasmas, and for the guiding center (2,1), (2,2), and low-frequency (3,0) modes in very prolate plasmas. In these limits a theory based on elastic moduli loses its validity since any such theory assumes a large effective wavelength compared to the interparticle spacing.

However, Eqs. (3.7) fail to capture the frequency shift for plasmas at finite Γ . Here the data are more difficult to obtain since modes damp rather rapidly, thermal fluctuations are larger, and the frequency shifts are small. However, it is apparent from Fig. 6 that as $1/\Gamma$ increases there is a positive frequency shift for the (2,0) mode in a guiding center spherical plasma. We have also performed finite Γ simulations for some nonspherical plasmas, which display a different dependence of the frequency shift on Γ [see Fig. 6(a)].

The rather scattered frequencies displayed in Fig. 6(a) can be explained using the predictions of Eqs. (3.6). Equation (3.6a) predicts how the frequency shifts depend on the modulus $\kappa + 4/3\mu$. Thus each data point of Fig. 6(a) can be employed to determine an empirical value of $\kappa + 4/3\mu$ as a function of Γ . The equilibrium pressure p is also required in this analysis; however, it is a known function of Γ , given by Eq. (2.6). The empirical results for $\kappa + 4/3\mu$ are displayed in Fig. 7(a). The scattered frequency shift data of Fig. 6(a) have collapsed onto a single curve in Fig. 7(a). Thus the frequencies of the (2,0) mode in plasmas of different shapes and sizes provide consistent results for $\kappa + 4/3\mu$.

The theoretical prediction of Eq. (3.7a) for the dependence of $\kappa + 4/3\mu$ on Γ is also displayed in Fig. 7(a). While the prediction works well at large Γ , at smaller Γ values there is a discrepancy due to a well-known problem with Eqs. (3.7). Equations (3.7) imply $\kappa + 4/3\mu \rightarrow 0$ as $\Gamma \rightarrow 0$, whereas it is known that $\kappa + 4/3\mu \rightarrow \gamma n_0 kT$ for a uniform weakly correlated plasma. Although rather complex theoretical models that avoid this discrepancy have been constructed [32], here we observe that a better fit to the data is obtained if one replaces Eq. (3.7a) by the *ad hoc* expression. [In fact, there is some theoretical justification for Eq. (3.8) on the basis of a sum rule; see Ref. [13].]

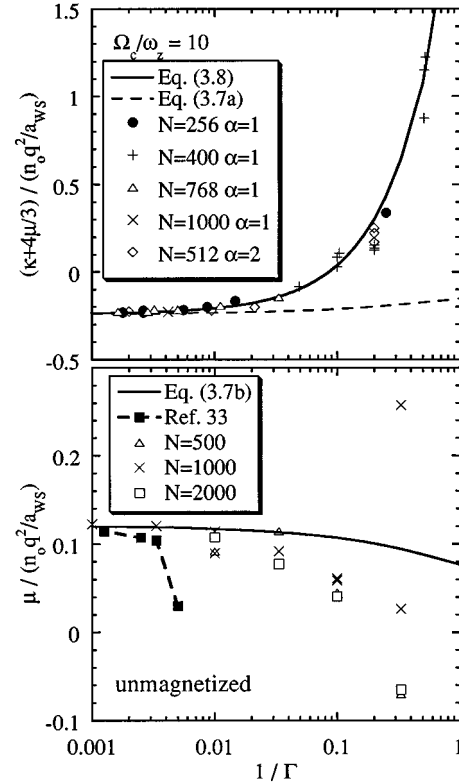


FIG. 7. Moduli extracted using the data of Fig. 6 and the predictions of Eqs. (3.5a) and (3.6a). The upper plot depicts the combination $\kappa + 4\mu/3$ for a guiding center plasma. The plot also compares the simulation data to the theory predictions of Eqs. (3.7a) and (3.8), with $\gamma=2.5$. The lower plot depicts the shear modulus μ extracted from the unmagnetized simulations. The solid line is the prediction of Eq. (3.7b) and the connected solid squares are the predictions for the low-frequency limit of μ from Ref. [33].

$$\kappa + \frac{4}{3}\mu = \frac{4}{15}n_0 \frac{U}{N} + \gamma n_0 kT, \quad (3.8)$$

where one would expect $\gamma=3$ in the weakly correlated limit for the one-dimensional adiabatic compressions and expansions associated with the guiding center (2,0) plasma mode. The data of Fig. 7(a) show that Eq. (3.8) is in reasonably close agreement to the simulation results, although setting $\gamma=2.5$ provides a better fit than $\gamma=3$.

A frequency shift is also predicted for an unmagnetized (2,0) mode in a spherical plasma. According to Eqs. (3.5a), (3.7b), (3.2), and (2.6), the shift should be given by $N^{2/3}(\Delta\omega_{20}/\omega_2) = (\sqrt{10}/3/\Gamma)$, but this does not match the data, which show almost no shift (Fig. 7). This suggests that there are temperature-dependent corrections to the shear modulus μ beyond Eq. (3.7b), just as there were corrections for $\kappa + 4/3\mu$. Indeed, such finite Γ corrections to the low-frequency form of the shear modulus have been discussed previously [33], but as far as we know there has been little theoretical work on the high-frequency limit. However, one would expect on intuitive grounds that the high-frequency shear modulus would be larger than the low-frequency modulus, since even a liquid can have an elastic response to high-frequency shear.

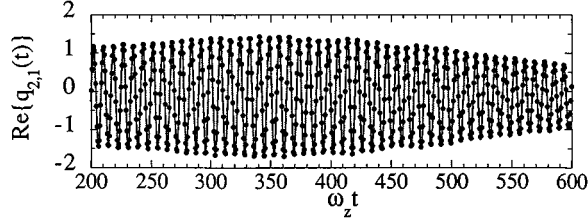


FIG. 8. Real part of the quadrupole moment q_{21} as a function of time for an initially spherical cloud of $N=50$ ions with $\Gamma=\infty$, with a (2,1) guiding center mode perturbation added. The solid curve is the result of a strongly magnetized molecular-dynamics simulation with $\Omega_b/\omega_z=10^5$. Dots are the prediction from a linear superposition of the exact guiding center crystal eigenmodes, which follow from a numerical solution of Eq. (3.9).

The frequency shift data from Fig. 6(b) can be employed empirically to determine the shear modulus μ using Eq. (3.5a) and the known form of the equilibrium pressure p , Eq. (2.6). The results are summarized in Fig. 7, which also shows the prediction for μ from Eq. (3.7b), as well as the low-frequency form from Ref. [33]. Although the errors are rather large at low Γ , the high-frequency form for μ obtained from our simulations is larger than the low-frequency prediction of Ref. [33], and appears to remain finite even in the fluid phase, as expected. However, for low Γ values, our results for μ appear to be somewhat smaller than the prediction of Eq. (3.7b), although scatter in the data is too large to make a conclusive statement.

5. Amplitude variation and exact crystal eigenmodes

In addition to frequency shifts the amplitude of the normal modes is sometimes observed to vary with time; generally this variation is slow compared to the mode frequency. We have found that this amplitude variation is due to two effects. The first effect stems from the choice of the initial conditions in the simulation, as well as the finite size of the cloud; the second is intrinsic to the plasma and is due to collisional viscous damping of the mode. An example of the first type of amplitude variation is displayed in Fig. 8. A crystallized spherical cloud of 50 charges is initially excited with a (2,1) mode perturbation according to Eqs. (3.3) and Table I of Ref. [10], taking the strong magnetic field limit $\Omega_c/\omega_z=10^5$. The amplitude of the real part of q_{21} is first observed to increase, then decrease. This complex amplitude variation stems from the fact that for a crystallized system any small perturbation is a sum of exact crystal eigenmodes. The (2,1) fluid mode perturbation that we used as the initial condition is nearly an exact eigenmode, but more than one exact eigenmode contributes, and since these modes have different frequencies a complex time variation results.

Although the crystal is amorphous, the equilibrium positions of the ions are known, so one can determine the exact strongly magnetized eigenmodes of the 50-ion crystal. Since motions only along z are allowed in this limit, these strongly magnetized eigenmodes satisfy the equation

$$M\omega^2\delta z_i = \sum_{j=1}^N \frac{\partial\Phi}{\partial z_i^{(0)}\partial z_j^{(0)}} \delta z_j, \quad (3.9)$$

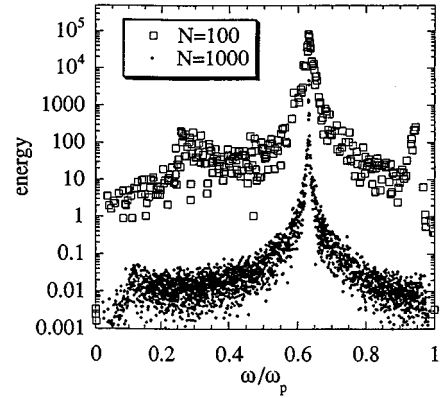


FIG. 9. Degree to which different exact unmagnetized eigenmodes are excited by an unmagnetized (2,0) perturbation in spherical clouds of two different sizes. The energy in each eigenmode is plotted vs the mode frequency. The energy scale is in arbitrary units with an offset chosen for one data set in order to place both sets on the same graph without overlap.

where Φ is the potential energy of the crystallized equilibrium, $z_i^{(0)}$ is the equilibrium position of the i th charge, and δz_i the change in position due to a mode. Thus the mode frequencies are the eigenvalues of an $N\times N$ matrix, so there are N guiding center modes. [In fact, there are as always $3N$ exact eigenmodes, but the other $2N$ modes are $\mathbf{E}\times\mathbf{B}$ drift modes and upper hybrid modes which are thrown away in Eq. (3.9).] We have solved for the eigenvalues and eigenvectors numerically, and then used these eigenmodes to determine the time evolution of the (2,1) multipole moment as predicted by a linear superposition of the exact modes, starting with the same initial (2,1) perturbation as was used in the molecular-dynamics simulation of Fig. 8. This evolution is displayed as the dots in Fig. 8; one can see that the evolution of $q_{21}(t)$ predicted by the exact crystal eigenmodes and by molecular dynamics agree well. This indicates that the amplitude variation observed in Fig. 8 is not due to dissipation, since the harmonic oscillator equations governing the dynamics for each eigenmode are integrable, so the evolution is reversible. Rather, the amplitude variation arises from the phase mixing of exact eigenmodes with slightly different frequencies.

We have observed that as the size of the crystal increases, the variation in the amplitude of the oscillation decreases. This implies that the (2,1) fluid mode approaches one of the crystal eigenmodes in the large N limit. This phenomenon is displayed directly for a different mode in Fig. 9. Here we show the energy excited in each exact eigenmode for an unmagnetized (2,0) fluid perturbation of a spherical cloud, as given by Eq. (3.4b). The unmagnetized eigenmodes are determined by numerically solving the unmagnetized eigenvalue equation $M\omega^2\delta\mathbf{x}_i = \sum_j \nabla_i^{(0)} \nabla_j^{(0)} \Phi \cdot \delta\mathbf{x}_j$. In Fig. 9 we have analytically averaged the energy in each exact mode over a set of equilibria obtained by all possible rotations of the given spherical equilibrium, in order to obtain results which are more or less independent of details of the particular equilibrium configuration. As N increases, the distribution of exact eigenmodes contributing to the (2,0) fluid perturbation becomes more sharply peaked around the fluid

frequency $\omega = \sqrt{6/5}\omega_z$. The detailed shape of this resonance curve is not presently understood theoretically, but the sharpness of the peak indicates that for large N only a few nearly degenerate modes contribute. Thus the fluid mode is nearly an exact eigenmode, and so there is little amplitude variation. However, for smaller N more exact eigenmodes contribute to the fluid perturbation and the fluid mode amplitude variation is larger. This effect does not occur in homogeneous systems with periodic boundary conditions, where both fluid and exact eigenmodes have the same spatial dependence, of the form $\exp(i\mathbf{k}\cdot\mathbf{x})$, independent of the system size.

One might ask why we do not excite a single-crystal eigenmode rather than the fluid perturbation, which is a superposition of the exact eigenmodes. First, for large clouds there is little difference between these two cases, as one can see from Fig. 9. Second, the exact crystal eigenmodes are meaningful excitations only in the crystal phase, whereas the fluid modes persist even in the weakly correlated regime (although they may be damped). In this sense the fluid excitations are more general.

Nevertheless, some insight into the dynamics of the strongly correlated cloud does follow from a brief examination of properties of the exact eigenmodes. For an unmagnetized plasma there are $3N$ exact eigenmodes with frequencies in the range $0 \leftrightarrow \omega_p$. The frequencies obey the Kohn sum rule, written for an amorphous OCP system as $\sum_{i=1}^{3N} \omega_i^2 = N\omega_p^2$, where ω_i is the frequency of the i th exact eigenmode. In Fig. 10 we display the normalized density of states $n(\omega)$ of the exact unmagnetized eigenmodes, defined by the relation $3N n(\omega)\Delta\omega/\omega_p =$ the number of modes with frequencies in the range ω to $\omega + \Delta\omega$. Here we take $\Delta\omega = 0.02\omega_p$, and consider a spherical unmagnetized plasma of $N=1000$ charges. There are three peaks in the distribution. The modes in the peak near $\omega \approx 0.3$ are predominantly torsional oscillations, which consist of shearing motions that do not change the shape or density of the cloud. Such modes have zero frequency in fluid theory, since the only restoring force to such motions stems from the finite shear modulus. The lowest frequency modes in this class are three $\omega=0$ modes corresponding to pure rotations of the spherical plasma. Similar shear modes are also observed in the homogeneous fcc and bcc densities of states, shown for comparison in the lower half of Fig. 10. We will return to these torsional modes in Sec. IV.

The class of modes in the peak near $\omega = \omega_p$ are bulk plasma oscillations modified by correlations. Such modes also exist in the infinite homogeneous system, as one can see in Fig. 10. For the spherical cloud, the highest frequency mode has $\omega = \omega_p$ exactly, and is in fact the breathing oscillation discussed in Appendix B and at the end of this section.

However, there is a sharp peak at intermediate frequencies in the density of states for the cloud which does not appear in the infinite homogeneous system. This peak is a consequence of surface plasma oscillations, which have a dispersion relation given by Eq. (3.2) for a spherical cloud. This dispersion relation leads to a divergence in $n(\omega)$ at the surface plasma frequency $\omega_p/\sqrt{2}$. The divergence is cut off when the mode wavelength becomes on the order of the interparticle spacing. The density of states predicted from Eq. (3.2) is shown in Fig. 10 for comparison.

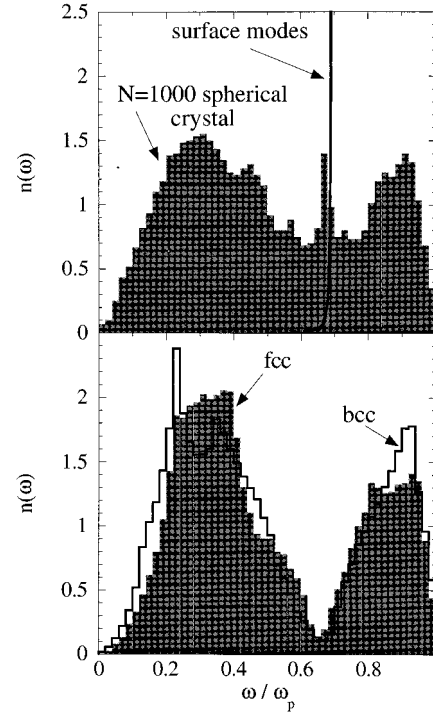


FIG. 10. Upper plot depicts the normalized density of states $n(\omega)$ for the exact unmagnetized eigenmodes of an $N=1000$ spherical cloud, as defined in the text. The superimposed solid curve in the upper plot depicts the density of states predicted by Eq. (3.2) for the surface modes. The lower plot depicts the normalized density of states for the modes of an infinite homogeneous unmagnetized crystallized OCP. The solid curve is for a bcc lattice, the gray region is for an fcc lattice.

6. Viscous damping

We now turn to the second type of amplitude variation, damping due to collisional viscosity of the plasma. Unlike the amplitude variation due to phase mixing discussed previously, this damping is an irreversible process. An example is displayed in Fig. 11. A guiding center (2,0) mode is excited in a spherical cloud. In this figure the kinetic energy of the cloud is plotted as a function of time. The kinetic energy oscillates as the cloud compresses, and expands along the magnetic field. In the upper figure Γ is large, $\Gamma \sim 10^5$, and there is almost no amplitude variation in the oscillations. This is because we have chosen $N=768$, which is sufficiently large so that the initial perturbation is nearly an exact crystal eigenmode.

However, if the initial cloud is at higher temperature, with $\Gamma=90$, substantial damping of the (2,0) mode now occurs (the lower figure). This behavior differs from the previously discussed amplitude variation due to phase mixing. Now the dynamics is not integrable, the evolution is irreversible, and true equipartition between the degrees of freedom is the eventual result. This energy equipartition does not occur if there is only phase mixing between uncoupled eigenmodes as in Fig. 8, since the energy in each exact eigenmode remains fixed. The first stages of equipartition can be observed in the lower half of Fig. 11. The random kinetic energy of the cloud increases, since the total energy is conserved as the mode damps. The temperature increase can be observed

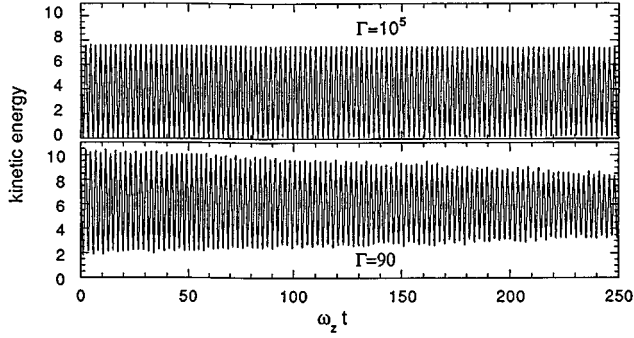


FIG. 11. Damping of (2,0) mode due to viscosity in a cloud of $N=768$ charges, guiding center simulation with $\Omega_c = 10\omega_z$. The kinetic energy of the cloud is plotted as a function of time. (a) Initially $\Gamma \sim 10^5$, and almost no damping of the mode is observed. (b) Initially $\Gamma = 90$; now the mode damps and the cloud heats.

through the increase in the minimum kinetic energy achieved during an oscillation. This represents an irreversible transfer of energy from the normal mode to random thermal motion. Eventually, the mode amplitude decays to a level set by thermal fluctuations.

The rate of mode damping as a function of the initial correlation parameter is displayed in Fig. 12(a). The damping rate γ is defined by fitting the observed decay of the amplitude of $q_{20}(t)$ to an exponential form

$$q_{20}(t) = A \exp(-\gamma t) \sin(\omega_{\text{sim}} t).$$

For $\Gamma < 10$ the mode damping cannot be determined unambiguously due to amplitude variations caused by thermal

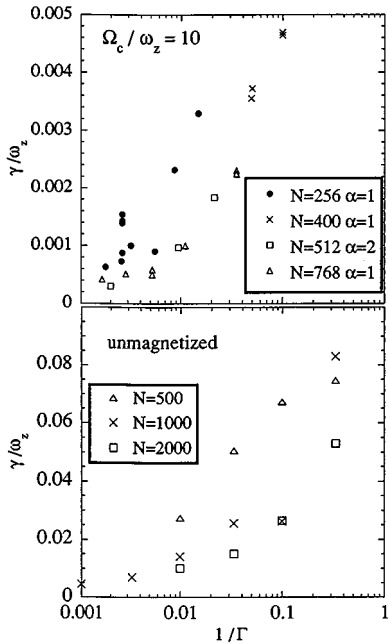


FIG. 12. Damping rate γ of the (2,0) normal mode in spheroidal cloud simulations of different sizes and shapes as a function of temperature (inverse correlation parameter $1/\Gamma$). The upper plot is for guiding center simulations, and the lower plot is for unmagnetized simulations.

noise (however, the real frequency can still be extracted with reasonable accuracy). For $\Gamma > 10$ the mode damping is observed to increase with increasing temperature (i.e., increasing $1/\Gamma$). Simulations of unmagnetized (2,0) modes in a spherical plasma also yield a damping rate which increases with increasing temperature [Fig. 12(b)].

An increase in collisional viscosity as temperature increases is opposite to what one observes in a weakly correlated plasma, where the collision frequency scales at $T^{-3/2}$ (i.e., $\Gamma^{3/2}$). However, in strongly correlated plasmas the increase of damping with temperature is expected, since in the crystalline phase waves are less damped than in the liquid phase, where collisional viscosity is larger. Indeed, this behavior has been observed in previous simulations of homogeneous strongly correlated systems [13], but has not yet been observed in actual experiments on three-dimensional strongly correlated plasmas.

Since the plasma temperature increases as the mode damps, and mode frequencies and damping rates are functions of Γ , some care was taken to extract frequencies and damping rates only during the initial stages before appreciable heating occurred. In addition, some simulations were repeated with different perturbation amplitudes to test the effect of plasma heating on our frequency extraction algorithms.

The damping of the modes can be employed to obtain information concerning transport coefficients of the correlated plasma. Equations (3.5) and (3.6) provide frequency shifts depending on the bulk and shear moduli κ and μ . These moduli need not be real, and their imaginary parts will induce mode damping. The imaginary parts of κ and μ can be related to the coefficients of bulk and shear viscosity in the relaxation time approximation of Maxwell [34]; however, these transport coefficients depend on mode frequency and magnetic field, and our review of the literature has not uncovered any concrete theoretical predictions for these high-frequency viscosities in a strongly correlated and possibly strongly magnetized plasma. On the other hand, the simulation results can be employed to obtain some information concerning these transport coefficients. In Fig. 12(a) the damping of the (2,0) guiding center mode for clouds of different sizes and shapes is plotted. Each datum provides a result for $\text{Im}(\kappa + 4/3\mu)$ through Eq. (3.5a); the results are shown in Fig. 13(a). Note that the scattered data of Fig. 12(a) collapse onto a single curve in Fig. 13(a). Thus the damping of guiding center (2,0) modes in clouds with different sizes and shapes provides consistent results for $\text{Im}(\kappa + 4/3\mu)$ in a guiding center plasma. This indicates that our perturbation theory based on bulk and shear viscosities is a useful approach to understanding the damping of this mode, just as the theory based on bulk and shear moduli was useful in explaining frequency shifts.

Similarly, unmagnetized (2,0) simulations can be employed to obtain $\text{Im}(\mu)$ using Eq. (3.5a) and the data of Fig. 12(b). The result for $\text{Im}\mu$ as a function of correlation parameter in an unmagnetized plasma is shown in Fig. 13(b). As expected, the shear viscosity of the plasma increases as Γ decreases, although the data become less reproducible at large values of $1/\Gamma$.

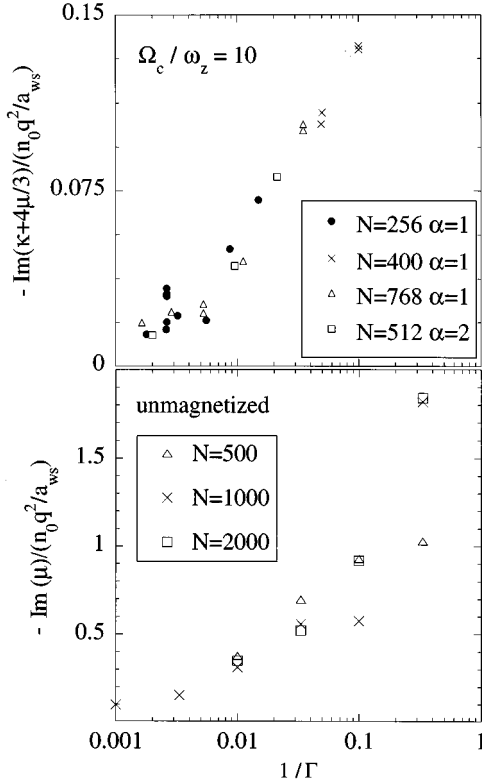


FIG. 13. Imaginary moduli obtained from the (2,0) mode damping of Fig. 12. The upper plot depicts the imaginary part of the modulus $(\kappa + 4/3\mu)$ from the guiding center damping data of Fig. 12 (upper plot), using Eq. (3.6a). The lower plot depicts the imaginary part of μ from unmagnetized (2,0) simulation of Fig. 12 (lower plot), using Eq. (3.5a).

7. Breathing mode

Finally, we examine one of the unmagnetized bulk plasma oscillations. Recall that in fluid theory there are an infinite number of degenerate bulk oscillations at the plasma frequency [see the discussion following Eq. (3.2)]. In a spherical plasma, one of these bulk oscillations is a breathing mode with radial displacements of the plasma proportional to spherical radius \mathbf{r} : $\delta\mathbf{v} = C\mathbf{r}\hat{\mathbf{r}}$ (see Fig. 2). This particular mode also happens to be an exact crystal eigenmode; in fact it is the highest frequency exact eigenmode, with $\omega = \omega_p$ exactly; see Appendix B and the discussion associated with Fig. 10.

This breathing mode has been simulated in a crystallized spherical plasma and, as expected, the frequency is observed to equal the plasma frequency to a few parts in 10^5 , and there is a negligible damping of the mode. However, at finite temperature there is a frequency shift, as well as a damping of this mode, shown in Fig. 15. The data are rather scattered, but they do indicate a positive frequency shift and damping, both of which increase with increasing $1/\Gamma$. This is in qualitative agreement with the results of the viscoelastic approximation for this mode, discussed in Ref. [10]. In this reference an approximate form for the frequency shift of this breathing mode is derived:

$$\Delta\omega = \frac{5}{2} \omega_p \frac{\{-4p + 3\kappa\}}{Mn_0\omega_p^2 R^2}, \quad (3.10)$$

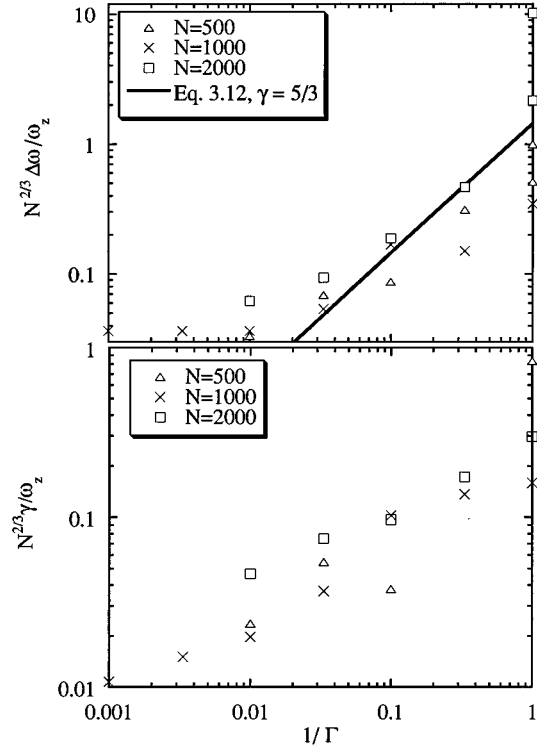


FIG. 14. Frequency shift $\Delta\omega$ and damping rate γ of the bulk plasma breathing mode in unmagnetized spherical clouds as a function of the correlation parameter Γ . The solid curve is the theory prediction of Eq. (3.12).

where R is the radius of the spherical plasma.

If we use Eq. (2.6) for p and Eq. (3.7) for κ in Eq. (3.10), we find that in the large Γ limit $\Delta\omega = 0$, in agreement with the exact crystal eigenmode analysis. However, at finite temperature Eqs. (3.10) and (3.7) yield results in disagreement with the simulations, so we modify the finite Γ form for κ in the spirit of Eq. (3.8):

$$\text{Re}(\kappa) = \frac{4}{9} n_0 \frac{U}{N} + \gamma n_0 kT, \quad (3.11)$$

where now we expect γ to be $\frac{5}{3}$ for small Γ in an unmagnetized plasma undergoing three-dimensional spherically symmetric compressions. Using Eq. (3.11) in Eq. (3.10) yields the following frequency shift:

$$N^{2/3} \text{Re}(\Delta\omega) = \frac{5}{2} \omega_p (\gamma - 4/3) / \Gamma = \frac{5}{6} \omega_p / \Gamma. \quad (3.12)$$

This shift is in qualitative agreement with the simulation results, shown in Fig. 14, although the simulation results are rather scattered. Both the real and imaginary parts of κ for an unmagnetized plasma could also be extracted from Fig. 14, using Eq. (3.10). However, the data are not very reproducible, particularly for $N = 500$, so we do not go through this exercise here.

IV. RESULTS FOR TORSIONAL MODES

Torsional modes of oscillation were studied in unmagnetized simulations of a crystallized plasma. A torsional dis-

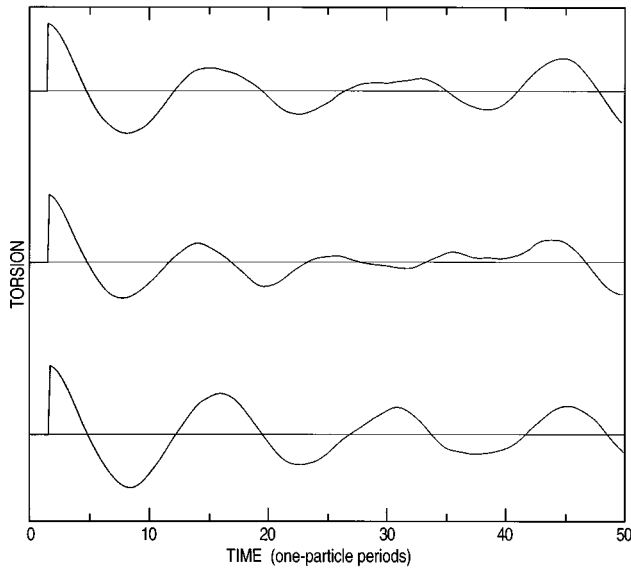


FIG. 15. The amplitude of torsional oscillations as a function of time in a crystallized ($\Gamma > 10^4$) plasma of 1000 ions. The initial step where the perturbation was imposed is visible at a time of about two one-particle periods. The three curves represent the behavior of the same initial cloud with the perturbation added about three perpendicular axes.

placement of a plasma cloud is an incompressible shear displacement and does not change the shape of the cloud. The perturbation has no effect on a cold fluid, and any restoring force is a measure of the elastic shear modulus of the strongly correlated plasma.

A cloud of 1000 ions in isotropic confinement was allowed to settle into its minimum configuration, and then a small torsional twisting motion by an angle $\Delta\phi$ was introduced about the z axis,

$$\Delta\phi = A \sin(z/R),$$

such that at $z=0$ the cloud was unperturbed; for positive z it was given a gradually increasing rotational velocity in one direction and for negative z in the other [see Fig. 2(f)]. The subsequent behavior of such oscillatory motion was studied. Figure 15 shows the initial behavior of the cloud after the perturbation, with the torsional motion of the ions calculated from their coordinates and velocities in the subsequent time development of the system. The period of the subsequent oscillation appears to be slow, on the order of 14 times the period of one ion oscillating in the confining field, and several such torsional modes appear to be excited.

To understand whether this is a general property, the above calculation was repeated about the two other perpendicular directions: the x and y axes, and the results are also shown in Fig. 15. To better compare this behavior, the motion of the cloud (for a period eight times longer than is shown in the figure) was Fourier analyzed, and the results of this are shown in Fig. 16. While the patterns of the frequencies extracted are not identical, all of them show a centroid at about 0.07 times the one-particle frequency—suggesting that this frequency is indeed a property of the correlated plasma, and that the detailed behavior is dependent on the specific

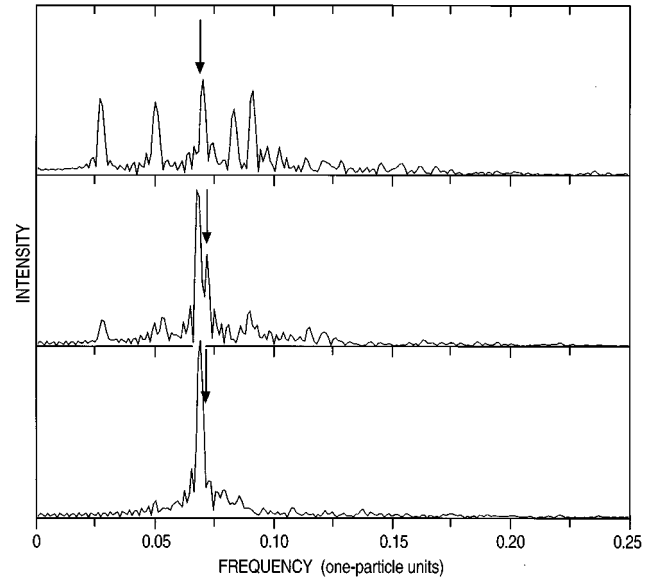


FIG. 16. Fourier transform of the full torsional oscillation simulations, some of which are partially displayed in Fig. 15. The results are summarized in Table II.

axes chosen, with respect to this particular finite plasma cloud. To better compare these, the mean frequency of each Fourier spectrum was extracted by multiplying each frequency component by the amplitude for this frequency obtained in the Fourier analysis. These mean frequencies are displayed as arrows on Fig. 16.

Since in the 1000-ion cloud the particles crystallize into individual shells, one can study the extent to which the restoring force in these torsional oscillations arises from interactions within one shell, or between shells. The simulations were modified so that torsional motion could be investigated within single shells. The outermost shell of the 1000-ion cloud has 384 ions. Therefore, in the simulations 384 ions were used, with the remainder of the cloud replaced by a central charge of 616 fixed at the origin. This resulted in a minimum-energy configuration slightly different from the outer shell of the 1000-ion system, but qualitatively the same. The shear oscillations in this shell were then studied, again with torsional displacements about three perpendicular axes and were repeated with the opposite sign for the initial perturbation. The results for the two signs were virtually identical, while the differences with choice of axis remained.

The results were again Fourier analyzed and are summarized in Table II, together with the results for the next two shells simulated in the same way. Again, no simple sharp frequency appears in these systems, and the mean frequency increases somewhat for the smaller shells. The complexity of the motion may perhaps be related to the fact that the density of eigenmodes in this low-frequency vicinity appears to be almost an order of magnitude lower than in the vicinity of the hydrodynamic modes (see Fig. 10) and the 1000-ion sphere has no simple symmetry with respect to the three axes.

An estimate of the uncertainties in the simulations is the fluctuations in the values from data about different axes; they are on the order of 10%. For the outer shell there are six values, corresponding to clockwise and counterclockwise ro-

TABLE II. Frequencies of torsional modes.

	outer shell	second shell	third shell	sphere
number of ions	384	273	175	1000
radius (a_{WS})	9.26	7.78	6.29	10.0
frequencies (ω_z)	0.059	0.076	0.093	0.071
	0.062	0.082	0.105	0.072
	0.083	0.092	0.070	0.069
	0.068			
	0.068			
	0.067			
mean (ω_z)	0.066	0.079	0.097	0.071
frequency \times radius ($\omega_z a_{\text{WS}}$)	0.61	0.61	0.59	0.71
estimate from Eqs. (4.1) ($\omega_z a_{\text{WS}}$)		0.75 (shells)		0.86 (sphere)

tations. The radii of the shells are extracted from the simulation, and for the full sphere the radius is that of an equivalent uniform charged sphere, $1000^{1/3} a_{\text{WS}} = 10 a_{\text{WS}}$ (the radius of the outer shell plus half the intershell spacing would yield the same value).

Estimates of the frequencies for such modes in spherical clouds have been made on the basis of the bulk shear modulus of the OCP, given by Eq. (3.7b). For a spherical cloud the frequency will depend on the radius R of the cloud [10, 16],

$$\omega = 2.50c/R \approx 0.86\omega_z a_{\text{WS}}/R \quad (4.1a)$$

for a full sphere where $c = \sqrt{\mu/Mn_0}$ is the shear sound speed of a homogeneous amorphous solid OCP. For a shell of radius R , a similar result holds:

$$\omega = 2c_{2D}/R \approx 0.75\omega_z a_{\text{WS}}/R, \quad (4.1b)$$

where $c_{2D} = \sqrt{\mu_{2D}/Mn_0}$ is the shear sound speed of a 2D amorphous OCP, and μ_{2D} is the shear modulus of such a plasma [35]. These equations predict that the product of the radius and frequency should be independent of the shell size, and this appears to be the case in the simulations. But the predicted value of this product is larger by about 18% than those extracted from the simulation. The frequency of the torsional oscillation times the radius of the sphere is larger than this product for the shells by the predicted amount—it differs from the estimate by essentially the same factor.

V. DISCUSSION

We have shown that under ideal conditions of molecular-dynamics computer simulations it is possible to extract information on bulk dynamical properties of the one-component plasma by measurement of frequency shifts and damping in low-order normal modes of trapped non-neutral plasmas. Since both the damping and the frequency shifts scale with particle number as $1/N^{2/3}$, in actual experiments the effects would be easier to observe in small clouds than in large clouds. However, if the clouds are too small, reproducibility of the results and their interpretation in terms of bulk properties of the OCP will be compromised. Our simulation results indicate that $N \geq 100$ is required for guiding center plasmas, and $N \geq 1000$ is required for unmagnetized plasmas, in

order to obtain reproducible data. It is not presently understood why there is more scatter in the unmagnetized results than in the guiding center results—it may be somehow connected to the greater number of degrees of freedom in unmagnetized plasma motions ($3N$ vs N for magnetized plasma motions at or below ω_p).

In the very strongly correlated limit $\Gamma \rightarrow \infty$ the frequency shifts in the modes were compared to the results of a theoretical model which treats the plasma as an elastic spheroid with bulk and shear moduli. Equilibrium correlation pressure distorts the shape of the spheroid, causing one contribution to this shift. The remainder of the frequency shift is due to the extra restoring forces arising from the bulk and shear moduli. When theoretical values for the high-frequency moduli of an amorphous OCP were employed in the model, good agreement with the observed shifts was obtained without adjustable parameters for both unmagnetized and guiding center plasma modes (Fig. 5).

For the (2,0) mode the frequency shifts were also observed to vary with Γ (Fig. 6). This variation was employed to extract finite temperature corrections to the high-frequency bulk modulus of a strongly magnetized OCP and the high-frequency shear modulus of an unmagnetized OCP (Fig. 7). As far as we know there are no other simulation results in the literature with which to compare these data.

Amplitude variation of the modes was also observed in the simulations. This variation was explained by two physical effects. One effect, due to the finite size of the plasma, was caused by phase mixing of the combination of exact crystal eigenmodes which contributed to a given fluid eigenmode. For sufficiently large clouds this effect was negligible. The other type of amplitude variation was explained by viscous dissipation in the strongly correlated plasma. Results for high-frequency bulk and shear viscosities as a function of Γ were extracted from the data on the damping of the modes using the aforementioned viscoelastic model (Fig. 13). In the unmagnetized limit the measured shear viscosity was found to be about an order of magnitude larger than the bulk viscosity measured under guiding center dynamics.

In simulations of an unmagnetized spherical plasma, a breathing mode of the plasma was also excited. This mode differs from the unmagnetized surface modes in that it is a pure compression of the plasma as opposed to an incom-

pressible change in the shape of the plasma. The mode corresponds to an unmagnetized bulk plasma oscillation with a wavelength of the order of the plasma size. An increase in the frequency shift and damping with increasing temperature was observed (Fig. 14). These effects may be compared to analogous effects seen in previous simulations which have measured the dynamic structure factor of a homogeneous unmagnetized OCP [13]. In these simulations a plasma peak in the structure factor is observed, whose frequency width and position vary with Γ in a manner that is qualitatively similar to the damping and frequency shift seen in our simulations.

Torsional modes of oscillation were observed in the unmagnetized simulations of a crystallized plasma. These torsional modes are incompressible shearing oscillations which do not change the shape of the cloud, but which instead rely entirely on the finite shear modulus of the system. As such these modes are sensitive measures of the shear modulus of the strongly correlated plasma, so it would be particularly interesting if these modes could be excited in real experiments. Unlike the surface plasma modes, the torsional modes cannot be easily excited in experiments by oscillation of the potentials on the external electrodes. However, it might be possible to excite these modes by means of the lasers which are used to control the rotation frequency of the ion cloud [21]. These lasers are typically directed through the edge of the cloud. Two such laser beams directed at the outer edges of the upper and lower parts of the cloud could be used to excite torsional oscillations. By varying the intensity of the laser light at the mode frequency, one could excite the oscillations while sweeping the rotation frequency through the Brillouin limit to create unmagnetized conditions in the rotating frame. Thus it may be possible to obtain a direct experimental measure of the unmagnetized shear modulus of a strongly correlated plasma.

ACKNOWLEDGMENTS

This work was supported by National Science Foundation Grant Nos. PHY91-20240 and PHY94-21318, Office of Naval Research Grant No. N00014-89-J-1714, and by the U.S. Department of Energy, Nuclear Physics Division, under Contract No. W-31-109-ENG-38.

APPENDIX A: SPHEROIDAL HARMONICS

The separable solution of Laplace's equation in spheroidal coordinates allows a generalization of spherical multipole moments which is of use in the diagnosis of the normal modes of a spheroidal plasma. The spheroidal multipoles follow from the expansion in spheroidal coordinates of the vacuum Greens function for Laplace's equation:

$$\frac{1}{|\mathbf{x}-\mathbf{x}'|} = \frac{1}{d} \sum_{l=0}^{\infty} \sum_{m \leq l} (-i)^m (2l+1) \times \left[\frac{(l-m)!}{(l+m)!} \right]^2 P_l^m(\xi_2') P_l^m(\xi_2) P_l^m(\xi_1^</d) Q_l^m(\xi_1^>/d) \times e^{im(\phi-\phi')}, \quad (\text{A1})$$

where we use spheroidal coordinate representations for \mathbf{x} and \mathbf{x}' , $\mathbf{x} = (\xi_1, \xi_2, \phi)$, $\mathbf{x}' = (\xi_1', \xi_2', \phi')$, d is the parameter of

the spheroidal coordinate system [see Eq. (3.5) of Ref. [10]], $\xi_1^</math> ($\xi_1^>$) is the smaller (larger) of ξ_1 and ξ_1' , P_l^m is a Legendre function of the first kind, and Q_l^m is a Legendre function of the second kind. We have chosen forms of the Legendre functions such that $P_l^m(x)$ is real on $x \in [-1, 1]$ and $Q_l^m(x) \rightarrow 0$ as $\text{Re}x \rightarrow \infty$.$

Using Eq. (A1) we write the potential $\Phi(\mathbf{x})$ due to a density distribution $n(\mathbf{x})$,

$$\Phi(\mathbf{x}) = q \int d^3x' \frac{n(\mathbf{x}')}{|\mathbf{x}-\mathbf{x}'|},$$

in terms of moments q_{lm} of the density:

$$\Phi(\mathbf{x}) = q \sum_{l,m} \frac{4\pi}{2l+1} c_{lm} q_{lm} Y_{lm}(\xi_2, \phi) Q_l^m(\xi_1/d). \quad (\text{A2})$$

Here,

$$Y_{lm}(\xi_2, \phi) = \sqrt{\frac{(2l+1)(l-m)!}{4\pi(l+m)!}} e^{im\phi} P_l^m(\xi_2)$$

is the usual spherical harmonic, c_{lm} is a coefficient chosen as

$$c_{lm} = \frac{(-i)^m 2^{l+1} \Gamma(l+3/2)}{\sqrt{\pi} d^{l+1} (l+m)!}$$

in order that Eq. (A2) approaches the usual expression [36] in the spherical limit $d \rightarrow 0$, and q_{lm} is a spheroidal multipole moment, defined as

$$q_{lm} = d_{lm} \int d^3x' n(\mathbf{x}') [Y_{lm}(\xi_2', \phi') P_l^m(\xi_1'/d)]^*, \quad (\text{A3})$$

where d_{lm} is another coefficient determined by our choice of c_{lm} :

$$d_{lm} = \frac{\sqrt{\pi} (l-m)! d^l (i)^m}{2^l \Gamma(l+1/2)}.$$

A given normal mode consists of a single oscillating multipole moment q_{lm} . This follows from Eq. (A2) as well as from the form of the potential ψ^{out} exterior to the plasma [see Eq. (3.6b) of Ref. [10]]. By recording the time evolution of this multipole moment in our simulations, we are then able to pick out a mode with given l and m for examination.

Furthermore, the multipoles have a relatively straightforward form in cylindrical coordinates. As discussed in connection with the form of the mode potential, the combination $Y_l^m(\xi_2, \phi) P_l^m(\xi_1/d)$ can be written as a finite power series in ρ and z . Some results for q_{lm} are displayed in Table III.

APPENDIX B: EXACT CRYSTAL EIGENMODES FOR SOME SPECIAL GEOMETRIES

In this appendix we consider some exact analytic solutions for the unmagnetized crystal eigenmodes of a trapped single-species plasma cooled to a crystalline state. The modes correspond to breathing motions of the crystal. There

TABLE III. Spheroidal multipole moments in cylindrical coordinates (ρ, ϕ, z) .

l	m	q_{lm}
0	0	$\frac{1}{2\sqrt{\pi}} \int d^3x' n(\mathbf{x}')$
1	0	$\frac{1}{2} \sqrt{3/\pi} \int d^3x' z' n(\mathbf{x}')$
1	1	$-\frac{1}{2} \sqrt{3/2\pi} \int d^3x' \rho' e^{-i\phi'} n(\mathbf{x}')$
2	0	$\frac{1}{12} \sqrt{5/\pi} \int d^3x' (6z'^2 - 3\rho'^2 - 2d^2) n(\mathbf{x}')$
2	1	$-\frac{3}{2} \sqrt{5/6\pi} \int d^3x' z' \rho' e^{-i\phi'} n(\mathbf{x}')$
2	2	$\frac{1}{4} \sqrt{15/2\pi} \int d^3x' \rho'^2 e^{-2i\phi'} n(\mathbf{x}')$
3	0	$\frac{1}{20} \sqrt{7/\pi} \int d^3x' z' (10z'^2 - 15\rho'^2 - 6d^2) n(\mathbf{x}')$
3	1	$-\frac{3}{40} \sqrt{7/3\pi} \int d^3x' (20z'^2 - 5\rho'^2 - 4d^2) \rho' e^{-i\phi'} n(\mathbf{x}')$
3	2	$\frac{15}{4} \sqrt{7/30\pi} \int d^3x' z' \rho'^2 e^{-2i\phi'} n(\mathbf{x}')$
3	3	$-\frac{5}{8} \sqrt{7/5\pi} \int d^3x' \rho'^3 e^{-3i\phi'} n(\mathbf{x}')$

are three cases where such modes can be described analytically.

1. Spherical cloud, $\beta = \alpha = 1$

The fully nonlinear equations of motion for the charges are

$$M\ddot{\mathbf{x}}_i = -\frac{\partial\Phi}{\partial\mathbf{x}_i}, \quad (\text{B1})$$

where the potential energy of the charges is

$$\Phi = \sum_i \left\{ \sum_{i>j} \frac{q^2}{|\mathbf{x}_i - \mathbf{x}_j|} + \frac{1}{2} M \omega_z^2 [z_i^2 + \beta(x_i^2 + y_i^2)] \right\}.$$

For $\beta = 1$, consider the transformation $\mathbf{x}_i = f(t)\mathbf{x}_i^{(0)}$, $f > 0$, where $\mathbf{x}_i^{(0)}$ is the equilibrium position, satisfying

$$\frac{\partial\Phi}{\partial\mathbf{x}_i^{(0)}} = 0. \quad (\text{B2})$$

Equation (B1) then becomes

$$M\ddot{f}\mathbf{x}_i^{(0)} = -\frac{q^2}{f^2} \frac{\partial}{\partial\mathbf{x}_i^{(0)}} \sum_{j \neq i} \frac{1}{|\mathbf{x}_i^{(0)} - \mathbf{x}_j^{(0)}|} - m\omega_z^2 f \mathbf{x}_i^{(0)}.$$

However, Eq. (B2) implies that we may factor out the terms depending on f to obtain

$$\left[M\ddot{f} + M\omega_z^2 \left(f - \frac{1}{f^2} \right) \right] \mathbf{x}_i^{(0)} = 0. \quad (\text{B3})$$

This nonlinear equation, when linearized around the equilibrium $f = 1$, describes radial breathing oscillations which satisfy

$$\delta\ddot{f} = -3\omega_z^2 \delta f.$$

Note that the frequency of oscillations $\sqrt{3}\omega_z$ equals the plasma frequency ω_p of the spherical equilibrium [see Eq. (2.3)].

2. Coulomb chain, $\beta \gg 1$

In the limit that $\beta \gg 1$, the equilibrium is a line of charges along the z axis, referred to as a Coulomb string or chain. Now we consider breathing oscillations of the form $z_i = f(t)z_i^{(0)}$. Since $x_i = y_i = 0$ during this motion, the analysis again leads to Eq. (B3), so these oscillations also have frequency $\sqrt{3}\omega_z$.

3. 2D disc equilibrium, $\beta \ll 1$

In the limit $\beta \ll 1$, the charges are nearly unconfined radially and form a 2D disc of charge in the x - y plane. Now we take $(x_i, y_i) = f(t)(x_i^{(0)}, y_i^{(0)})$, so that $z_i = 0$ at all times and the disc oscillates in radius. The analysis now leads to the equation

$$\ddot{f} = -\beta\omega_z^2 \left(f - \frac{1}{f^2} \right),$$

so the frequency of linear oscillations is $\sqrt{3\beta}\omega_z$. The frequency is small, of order $\sqrt{\beta}$, since the density of the disc is low, so restoring forces are small.

-
- [1] A. Rahman and J. Schiffer, *Phys. Rev. Lett.* **57**, 1133 (1986).
[2] D. H. E. Dubin and T. M. O'Neil, *Phys. Rev. Lett.* **60**, 511 (1988).
[3] H. Totsuji, in *Strongly Coupled Plasma Physics*, edited by F. Rogers and H. DeWitt (Plenum, New York, 1987), p. 19.
[4] S. L. Gilbert, J. J. Bollinger, and D. J. Wineland, *Phys. Rev. Lett.* **60**, 2022 (1988).
[5] D. J. Wineland *et al.*, *Phys. Rev. Lett.* **59**, 2935 (1987); M. G. Raizen *et al.*, *Phys. Rev. A* **45**, 6493 (1992); F. Diedrich *et al.*, *Phys. Rev. Lett.* **59**, 2931 (1987); G. Birkl, S. Kassner, and H. Walther, *Nature (London)* **357**, 310 (1992).
[6] See, for example, A. N. Trivelpiece and R. W. Gould, *J. Appl. Phys.* **30**, 1784 (1959); R. C. Davidson and N. Krall, *Phys. Fluids* **13**, 1543 (1970); A. Rahman and J. Schiffer, *Phys. Scr.* **T22**, 134 (1988).
[7] D. H. E. Dubin, *Phys. Rev. Lett.* **66**, 2076 (1991).
[8] D. J. Heinzen *et al.*, *Phys. Rev. Lett.* **66**, 2080 (1991); J. J. Bollinger *et al.*, *Phys. Rev. A* **48**, 525 (1993).
[9] M. D. Tinkle *et al.*, *Phys. Rev. Lett.* **72**, 352 (1994).
[10] D. H. E. Dubin, following paper, *Phys. Rev. E* **53**, 5268 (1996).
[11] J. J. Thompson, *Philos. Mag.* **7**, 237 (1904); E. Wigner, *Phys. Rev.* **40**, 749 (1932); E. Pollock and J. Hansen, *Phys. Rev. A* **8**, 3110 (1973).
[12] E.g., E. Salpeter and H. Van Horn, *Astrophys. J.* **155**, 183 (1969); or E. Schatzman, *White Dwarfs* (North-Holland, Amsterdam, 1958).
[13] J. P. Hansen, I. R. McDonald, and E. L. Pollock, *Phys. Rev. A* **11**, 1025 (1975).

- [14] K. Golden, G. Kalman, and P. Wyns, *Phys. Rev. A* **46**, 3454 (1992).
- [15] A. E. H. Love, *Some Problems of Geodynamics* (Dover, New York, 1911).
- [16] P. Morse and H. Feshbach, *Methods of Theoretical Physics* (McGraw-Hill, New York, 1953), p. 1872; H. Lamb, *Proc. London Math. Soc.* **13**, 189 (1882).
- [17] W. Paul and H. Steinwedel, *Z. Naturforsch. A* **8**, 448 (1953).
- [18] F. M. Penning, *Physica* **3**, 873 (1936).
- [19] J. H. Malmberg and T. M. O'Neil, *Phys. Rev. Lett.* **39**, 1333 (1977).
- [20] J. J. Bollinger and D. J. Wineland, *Phys. Rev. Lett.* **53**, 348 (1984); L. Turner, *Phys. Fluids* **30**, 3169 (1987).
- [21] L. R. Brewer *et al.*, *Phys. Rev. A* **38**, 859 (1988).
- [22] D. H. E. Dubin, *Phys. Rev. A* **42**, 4972 (1990).
- [23] H. Nayara, Y. Nayata, and T. Nakamura, *Phys. Rev. A* **36**, 1859 (1987).
- [24] G. Stringfellow, H. DeWitt, and W. L. Slattery, *Phys. Rev. A* **41**, 1105 (1990).
- [25] J. R. Pierce, *Theory and Design of Electron Beams* (Van Nostrand, Princeton, 1954), p. 159; R. C. Davidson, *Theory of Nonneutral Plasmas* (Benjamin, New York, 1974), Chap. 3.2.
- [26] D. H. E. Dubin, *Phys. Rev. A* **40**, 1140 (1989); J. P. Schiffer, *Phys. Rev. Lett.* **70**, 818 (1993); D. H. E. Dubin, *ibid.* **71**, 2753 (1993).
- [27] R. C. Davidson, *Theory of Nonneutral Plasmas* (Ref. [25]), p. 8.
- [28] R. C. Davidson, *Theory of Nonneutral Plasmas* (Ref. [25]), p. 7.
- [29] D. Bohm and E. P. Gross, *Phys. Rev.* **75**, 1851 (1949).
- [30] M. C. Abramo and M. P. Tosi, *Nuovo Cimento B* **21**, 363 (1974).
- [31] L. Landau and E. M. Lifshitz, *Theory of Elasticity*, 3rd ed. (Pergamon, New York, 1986), p. 88.
- [32] See, for example, S. Ichimaru, *Rev. Mod. Phys.* **54**, 1017 (1982).
- [33] S. Ogata and S. Ichimaru, *Phys. Rev. A* **42**, 4867 (1990).
- [34] S. Ogata and S. Ichimaru, *Phys. Rev. A* **42**, 142 (1990).
- [35] This modulus can be derived from the results of the following papers in a manner similar to the derivation of Eq. (3.16b); K. Golden, G. Kalman, and P. Wyns, *Phys. Rev. A* **46**, 3463 (1992); H. Totsuji, *ibid.* **17**, 399 (1978).
- [36] J. D. Jackson, *Classical Electrodynamics*, 2nd ed. (Wiley, New York, 1975), p. 136.